ORIGINAL ARTICLE

Channel incision into a submarine landslide on a Carboniferous basin margin, San Juan, Argentina: Evidence for the role of knickpoints

Charlotte Allen[1] | Luz E. Gomis-Cartesio[2] | David M. Hodgson[1] | Jeff Peakall[1] | Juan-Pablo Milana[3]

[1]School of Earth and Environment, University of Leeds, Leeds, UK

[2]Equinor ASA, Oslo, Norway

[3]CONICET, Faculdad de Ciencias Exactas, Fisicas y Naturales, Universidad Nacional de San Juan, San Juan, Argentina

Correspondence
David M. Hodgson, School of Earth and Environment, University of Leeds, Leeds, LS2 9JT, UK.
Email: d.hodgson@leeds.ac.uk

Funding information
Natural Environment Research Council

Abstract

Emplacement of submarine landslides, or mass-transport deposits, can radically reshape the physiography of continental margins, and strongly influence subsequent sedimentary processes and dispersal patterns. Typically, progressive healing of the complicated relief generated by the submarine landslide occurs prior to progradation of sedimentary systems. However, subsurface and seabed examples show that submarine channels can incise directly into submarine landslides. Here, the evolution of a unique exhumed example of two adjacent, and partially contemporaneous, submarine channel-fills is documented. The channels show deep incision (>75 m), and steep lateral margins (up to 70°), cut into a >200 m thick submarine landslide. The stepped basal erosion surface, and multiple terrace surfaces, are mantled by clasts (gravels to cobbles) reflecting periods of bedload-derived sedimentation, punctuated by phases of downcutting and sediment bypass. The formation of multiple terrace surfaces in a low aspect ratio confinement is consistent with the episodic migration of knickpoints during entrenchment on the dip slope of the underlying submarine landslide. Overlying sandstone-rich channel-fills mark a change to aggradation. Laterally stacked channel bodies coincide with steps in the original large-scale erosion surface, recording widening of the conduit; this is followed by tabular, highly aggradational fill. The upper fill, above a younger erosional surface, shows an abrupt change to partially confined tabular sandstones with normally graded caps, interpreted as lobe fringe deposits, which formed due to down-dip confinement, followed by prograding lobe deposits. Overlying this, an up-dip avulsion induced lobe switching and back-stepping, and subsequent failure of a sandstone body up-dip led to emplacement of a sandstone-rich submarine landslide within the conduit. Collectively, this outcrop represents episodic knickpoint-generated incision, and later infill, of a slope adjusting to equilibrium. The depositional signature of knickpoints is very

different from existing models, but is probably reflective of other highly erosional settings undergoing large-scale slope adjustment.

1 | INTRODUCTION

Submarine landslides, or mass-transport complexes (MTCs), and submarine channel systems are common features in deep-water environments. The interactions of submarine channels and landslides play a key role in the behaviour of sediment gravity flows, and govern sediment dispersal patterns (Martínez-Doñate et al., 2021; Nardin et al., 1979; Piper & Normark, 1983; Pirmez & Flood, 1995; Tek et al., 2020). Changes in sediment supply and routing patterns as a result of the emplacement of a submarine landslide, the relief of the landslide deposit and the behaviour of sediment gravity flows are inherently complex (Alves, 2015; Martínez-Doñate et al., 2021).

Seismic reflection data and observations from modern systems provide information on the large-scale evolution of systems, which include (i) the formation of canyons through MTC failure (Nelson et al., 2011), (ii) the capture of channel systems within a slide scar (Bart et al., 1999; Kneller et al., 2016; Qin et al., 2017; Sylvester et al., 2012), (iii) the role of MTCs in channel avulsion (Ortiz-Karpf et al., 2015; Steventon et al., 2021), (iv) the initiation and propagation of erosional channel systems above an MTC (Bull et al., 2020; Qin et al., 2017; Zhao et al., 2019), including the role of knickpoint zones (Tek et al., 2021) and (v) the influence of MTC topography on planform and cross-sectional architecture of channel-levee systems (Jegou et al., 2008; Kremer et al., 2018; Moscardelli et al., 2006; Piper et al., 1997; Ward et al., 2018). Only exhumed systems permit flow-scale evolution and internal architecture to be investigated. Therefore, detailed field-based studies of submarine channels that incise into submarine landslides are essential in bridging the resolution gap to help improve understanding of the complex interactions of topography, sediment supply and flow processes, and support subsurface predictions of facies distributions. However, few outcrop studies have examined the interaction of submarine channels that incise into an underlying mass-transport deposit (MTD) (Masalimova et al., 2016; Tek et al., 2020), and outcrops with good 3D constraint of these relationships have not been documented previously.

The aim of this contribution is to document an MTD that was incised by two channels, exposed in north-west Argentina. Using detailed, high-resolution sedimentological and stratigraphic analysis, the objectives are to: (i) investigate the evolution of two channels that incise into the MTD; (ii) determine lateral and vertical variations in channel-fill architecture, including terrace deposits, (iii) develop models for channel formation and stratigraphic evolution and (iv) place the context of this outcrop in terms of basin-scale processes.

2 | REGIONAL CONTEXT

2.1 | Geological setting

The study area is situated in the western sub-basin of the pericratonic Palaeozoic Paganzo Basin (Figure 1A; Fernandez-Seveso & Tankard, 1995; Limarino et al., 2002). The tectonic setting remains contentious, with the basin type interpreted as a retroarc foreland basin (Limarino et al., 2006; Ramos, 1988), a rift basin (Astini et al., 1995; Milana et al., 2010), a strike-slip basin with elements of extension (Fernandez-Seveso & Tankard, 1995), or as a series of intermittently linked depocentres, with subsidence linked to subduction (Fernandez-Seveso & Tankard, 1995; Mpodozis & Ramos, 1989; Ramos et al.,1986; Salfity & Gorustovich, 1983). The infill of the Paganzo Basin is subdivided into four super-sequences (Guandacol, Tupe, and Upper and Lower Patquia formations) separated by major hiatuses within the Lower Carboniferous to Late Permian (Fernandez-Seveso & Tankard, 1995). The 1800 m thick Guandacol Formation is subdivided into four depositional sequences, compromising cyclic deposition of fan deltas and basinal turbidites that represent four phases of glacial advance and retreat (Fernandez-Seveso & Tankard, 1995). The glacial regime has been interpreted as temperate and wet-based grounded glaciers (Lopez Gamundi & Martinez, 2000; Pazos, 2002), associated with the generation of large volumes of subglacial sediments (Elverhøi et al., 1998; Milliman & Meade, 1983). The La Peña area is interpreted as a proglacial, irregularly shaped submarine slope system with kinematic indicators in successive MTDs that suggest a spread of transport directions from NE-to-WNW (Milana et al., 2010; Sobiesiak et al., 2017; Valdez Buso et al., 2019).
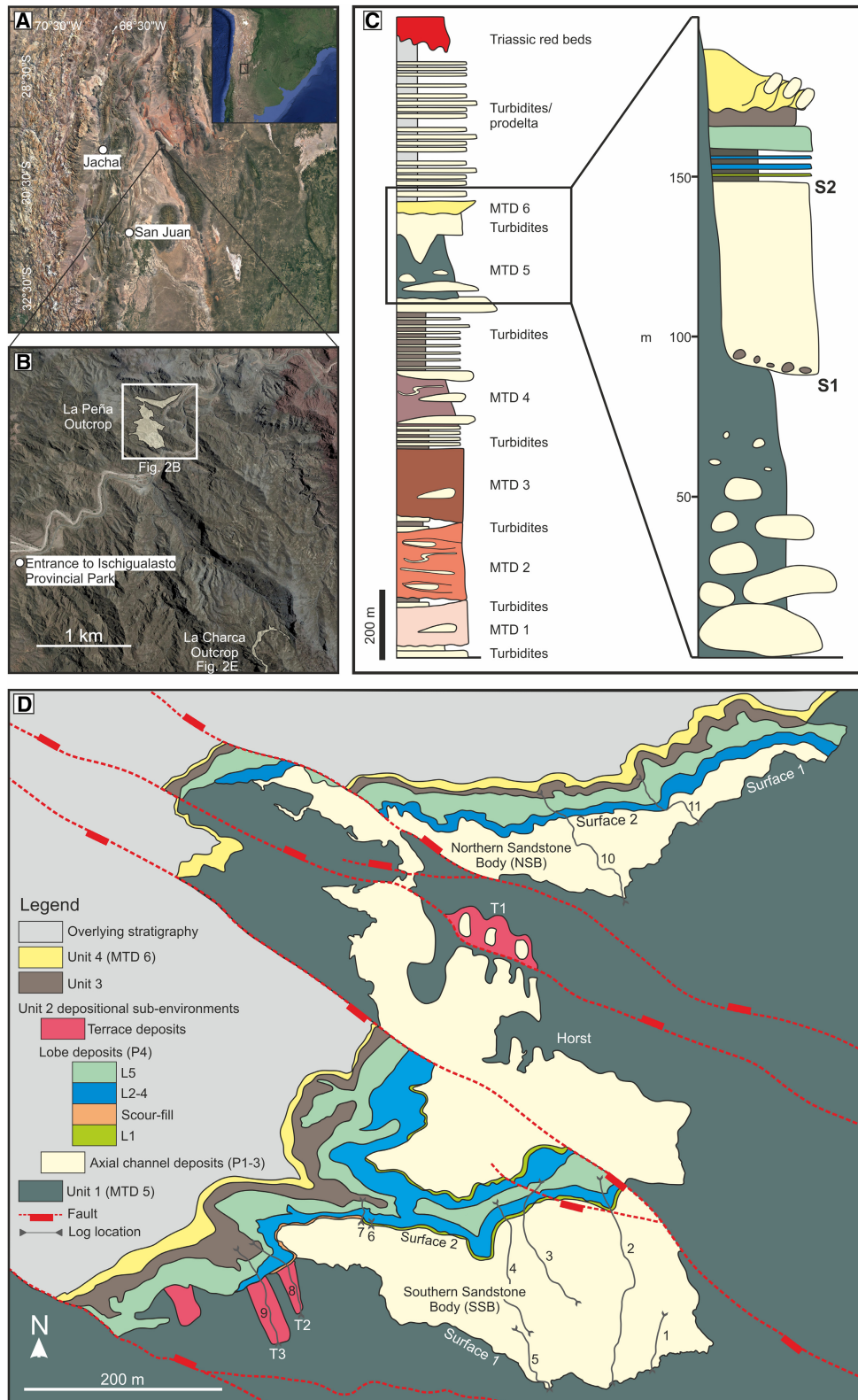
FIGURE 1 (A) Image of the Paganzo Basin, with inset showing location within South America. Study area is located within black box. (B) Enlargement of the study area, showing the location of the La Peña outcrops, where fieldwork was undertaken, and the La Charca outcrop, described using outcrop modelling and photographs. (C) Stratigraphic column (adapted from Valdez Buso et al., 2019), showing the regional stratigraphy, and La Peña stratigraphy in detail from data herein. (D) Geological map of the La Peña area, showing the deposits studied in this paper

2.2 | Study location

This study focusses on large exposures in the modern-day La Peña river valley within the Ischigualasto Provincial Park, on the border of San Juan and La Rioja provinces, north-western Argentina (Figure 1). The modern-day river valley incises into the western flank of the Ischigualasto and Caballo Anca ranges, part of an uplifted basement block related to the crustal scale Valle Fertil fault (Valdez Buso et al., 2019). The study area is cut by a number of NW-SE trending oblique normal faults, forming a horst structure in the central part of the study area (Figures 1D and 2A,B,C).

Five thick (150–220 m thick) MTDs, intercalated with packages of sand-prone turbidites, form *ca* 900 m of stratigraphy, overlain by fluvio-deltaics (Figure 1C), as part of the Guandacol Formation (Sobiesiak et al., 2017; Valdez Buso et al., 2019). The base of the studied succession is marked by a >200 m thick silt-prone MTD, with an erosive base and megaclasts, termed MTD 5 (Milana et al., 2010; Valdez Buso et al., 2019). The top of the studied succession is a *ca* 7 m thick, deformed sandstone-rich unit named MTD 6 (Milana et al., 2010; Valdez Buso et al., 2019). Two outcrops form the focus of this study: (1) La Peña outcrop (Figures 1 and 2A,B,C), trending NE-SW, comprising two sandstone bodies with erosional bases. The largest, to the south, herein termed the Southern Sandstone Body (SSB), is 400 m wide and

ca 75 m thick (Figure 2B). The Northern Sandstone Body (NSB) is *ca* 350 m wide and *ca* 60 m thick (Figure 2C), separated from the SSB by a horst block (Figures 1 and 2B,C). 2) The La Charca outcrop (Figure 2E,F; locations identified as E and F on Figure 2A), 2.5 km to the south-east, is described in this study using outcrop models and satellite imagery. Previous authors have interpreted these outcrops as recording ponded turbidites above topographic lows of the MTD (Kneller et al., 2016; Valdez Buso et al., 2019).

2.3 | Methodology

Eleven high-resolution (1:10–1:25 scale) composite sedimentary logs and numerous shorter logs were measured to document lithology, grain-size variation and sedimentary structures (total measured thickness: 363 m; Figures 3,4 and 5). Key stratal boundaries separating different facies groups and/or indicating erosion, were identified at outcrop (Figure 2B), registered on a detailed geological map (Figure 1) and aerial photographs. In combination with the sedimentary logs, the key surfaces were used to establish a correlation framework using lateral and vertical lithofacies relationships (Figures 1, 4 and 6). Palaeocurrent data (*n* = 291) were collected from ripple and climbing ripple cross-lamination, grooves and flutes, and orientation of erosion surfaces (Figures 4 and 6).
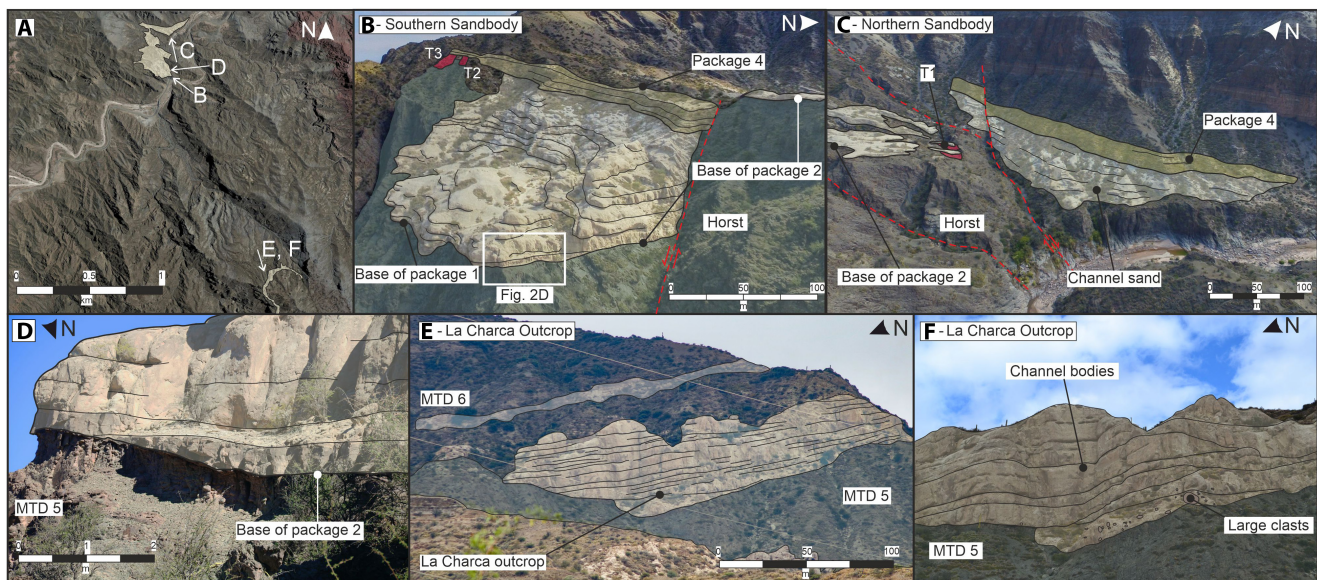
FIGURE 2 (A) Aerial photograph of the field area (used in Figure 1B) showing the relative location of outcrops, with arrows pointing to point of view of photographs in B, D, E and F. Outcrop images from (B) the Southern Channel of the La Peña outcrop. (C) The Northern Channel of the La Peña outcrop. (D) Contact between channel sand and MTD, in the Southern Channel of the La Peña outcrop, seen from the fault plane shown in (A). (E) Image of the up-dip La Charca outcrop (C), with line drawing overlay showing interpreted architecture. (F) Close-up of the La Charca outcrop, showing internal channel bodies and clast-rich basal layers. T1, T2 and T3 are terrace deposits

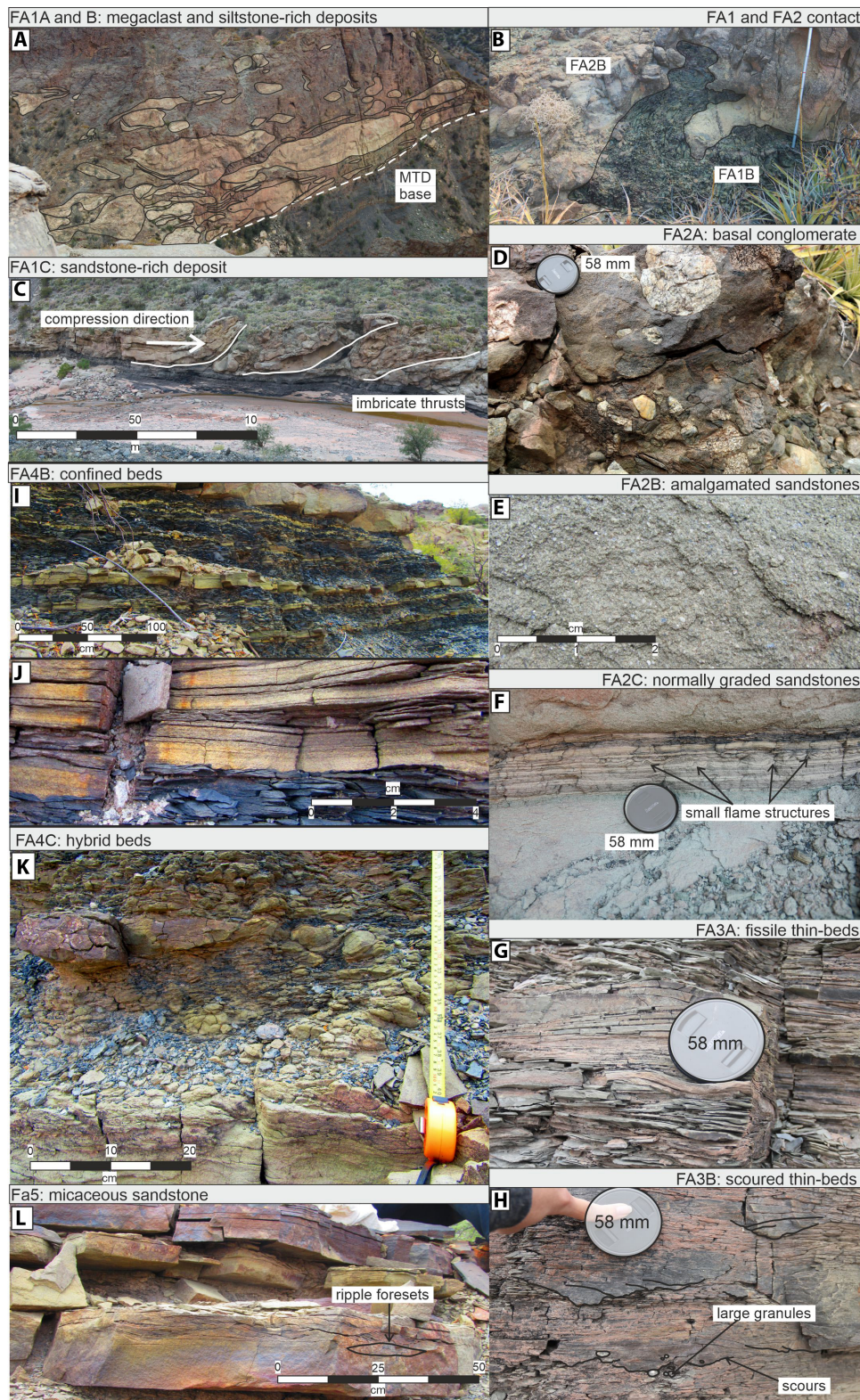**FIGURE 3**　Representative facies photographs from the La Peña section. (A) Lower sand block-rich, and mid sections of MTD 5, showing decreasing concentration of sand blocks up-strata. MTD basal contact with underlying stratigraphy is also seen. Field of view *ca* 100 m long. (B) Deformed contact between FA1B and overlying sandstone. Measuring stick is 0.8 m long. (C) Sand-rich imbricate thrust sheets of MTD 6. (D) Basal conglomerate layer from the Southern Channel. (E) Massive, amalgamated coarse-grained turbidite deposition. (F) Fine-grained sand bed cap of channelised bed geometries. (G) Fissile, thin-bedded terrace deposits. (H) Scoured and gravel-rich thin-bedded terrace deposits. (I) Repeated sand-mud couplets. (J) Sharp contact between sand and underlying mud. (K) Massive sandstone with overlying linked debrite. (L) Massive, planar and ripple laminated mica-rich sandstone
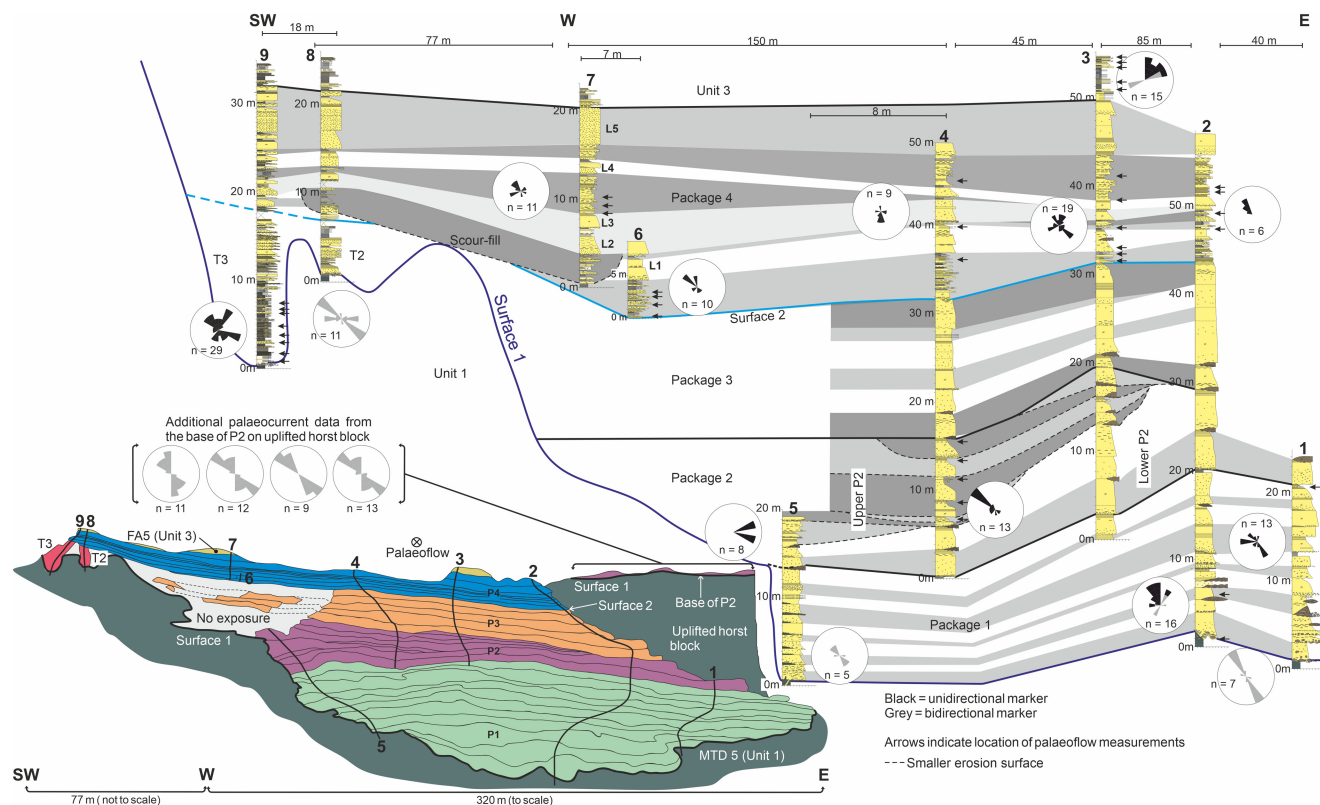
FIGURE 4 Correlation panel for SSB, and associated palaeocurrent data. Correlation panel is split into stratigraphic packages based on lithology and bed geometry. Additional palaeocurrent data are from an uplifted section of the SSB base. Outcrop line drawing shows location of sedimentary logs, and bed geometries within the Southern Channel. Note that the 77 m between the channel axis and the terraces are not to scale in order to fit these features onto the line drawing. The inset figure in the lower left is from a drone image of the 3D outcrop, so perspective is different. Furthermore, some beds are exposed at an angle and do not show true vertical thickness. The correlation panel is based on true thicknesses

3 | FACIES ASSOCIATIONS

Five facies associations have been identified and grouped based on interpreted processes and depositional environment, summarised in Table 1.

3.1 | Facies association 1: Remobilised deposits

3.1.1 | (A) Megaclast-rich poorly sorted deposit

Description: Heterogeneous packages up to 70 m thick (Figure 3A) with pale yellow medium-grained sandstone clasts, ranging from millimetre-scale stringers to >50 m diameter. The basal surface cuts step-wise into underlying sandstone turbidites by up to 5 m, and is immediately overlain by gravel layers (Valdez Buso et al., 2019). The concentration of clasts varies laterally and vertically, with zones of both clast and matrix-supported fabric, with an upward transition into matrix-supported dark green-grey,

poorly sorted siltstones with gravels and pebbles, both as layers and as isolated clasts (FA1B). Locally, clasts have sheared margins, exhibit internal contortion and preserve a range of disaggregation states. FA1A and FA1B share the same process interpretation (below) and were deposited as a single event.

3.1.2 | (B) Siltstone-rich poorly sorted deposit

Description: Comprises homogeneous, dark green-grey, poorly sorted siltstone matrix (Figure 3B), with rare pebbles and cobbles, and gravels dispersed throughout, with a range of extra-basinal and intra-basinal igneous, metamorphic and sedimentary lithologies. Commonly, sandstone clasts show evidence of shearing. Siltstones are folded and sheared, and locally cut by surfaces with abrupt changes in orientation of stratigraphy. The boundary between siltstone and overlying sandstone also exhibits loading, and wave-like geometries (Figure 3B). FA1B can be up to 150 m thick.
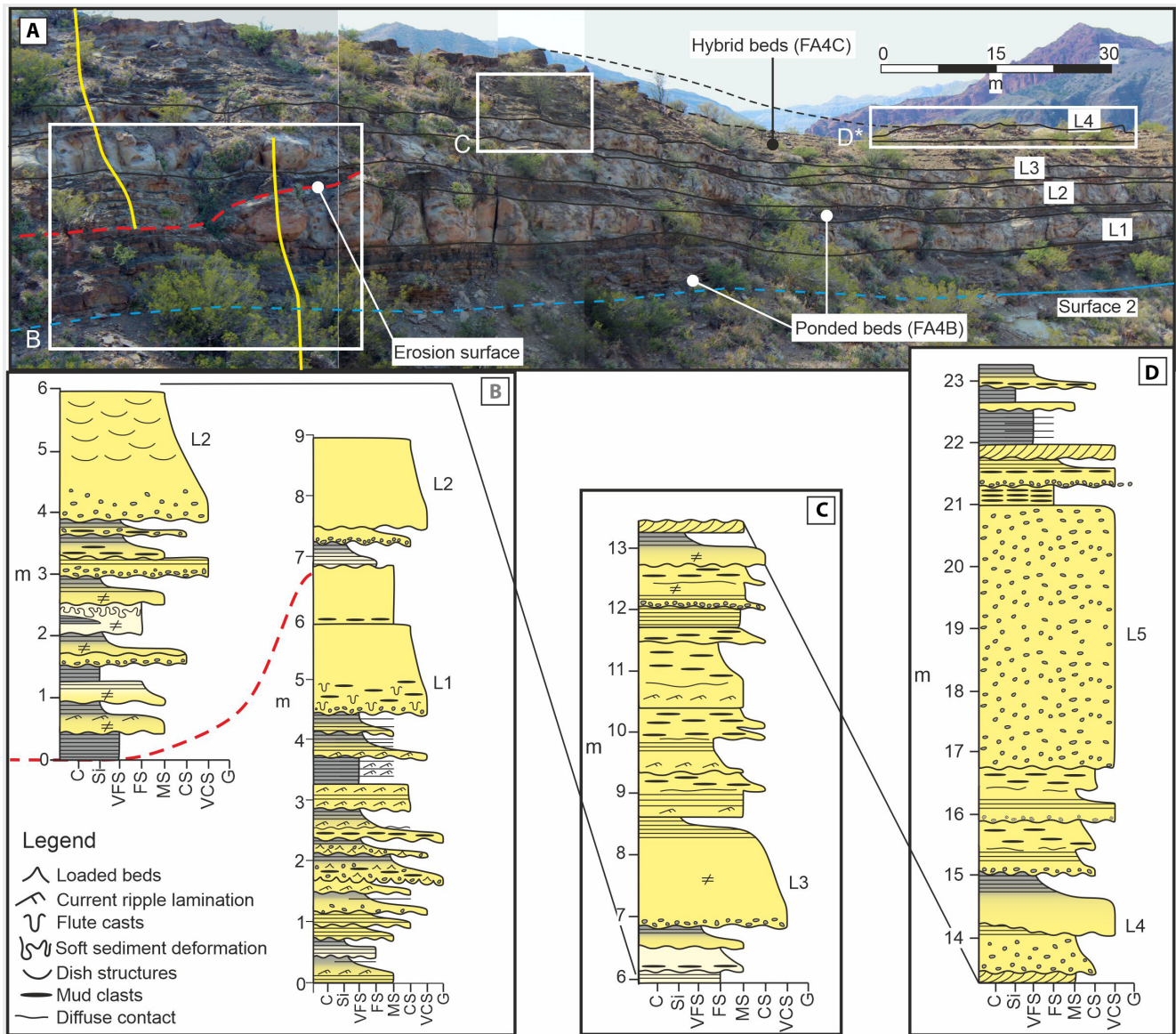
FIGURE 5 Outcrop image and sedimentary logs showing architecture and lithology of Package 4. (A) Panorama showing the western section of Package 4 within the channel axis. Lobes 1–4 are visible, as is the base of lobe 5. (B) Sedimentary logs showing the lateral change in lithology between the part of Package 4 containing L1, and the part where L1 has been truncated by a small channel, both of which are underlain by the first incidence of ponded sand-mud couplets. Top of log shows L2. (C) Log through the middle of Package 4, showing L3 and overlying hybrid bed deposition. (D) Sedimentary log through the upper section of Package, showing L4. D* Upper package of hybrid beds and L5 are not visible from this position as they are above the line of sight from this angle, but are included in (D)

Interpretation: The stepped basal surface, and evidence of shearing distributed throughout the deposit, and a matrix-supported and deformed fabric in the upper portion of the MTD, support interpretation of a debrite (Dott, 1963; Moscardelli et al., 2006; Nardin et al., 1979) emplaced in a single event that cut into the substrate. Previous authors have interpreted overpressure of pore fluids and hydroplaning along gravel layers at the base of the MTD as a mechanism for emplacement (Valdez Buso et al., 2019). The upper contact of FA1B is characterised by soft-sediment deformation and interpreted to indicate local liquefaction and fluidisation, cut by sandstone injectites.

3.1.3 | (C) Sandstone-rich deformed deposit

Description: Heterolithic deposit (*ca* 1 m thick) comprising medium-grained, yellow-grey sandstone beds with siltstone clasts distributed throughout (0.15–0.3 m thick), interbedded with siltstone layers. The overlying package (0.5–5 m thick) comprises grey-yellow-orange, medium to coarse-grained structureless sandstone, with rare small pebbles and gravels dispersed throughout. Laterally, the structureless sandstone transitions into blocky, imbricated sandstone sheets (Figure 3C) that comprise sets of thrust fault planes that dip *ca* 25°.
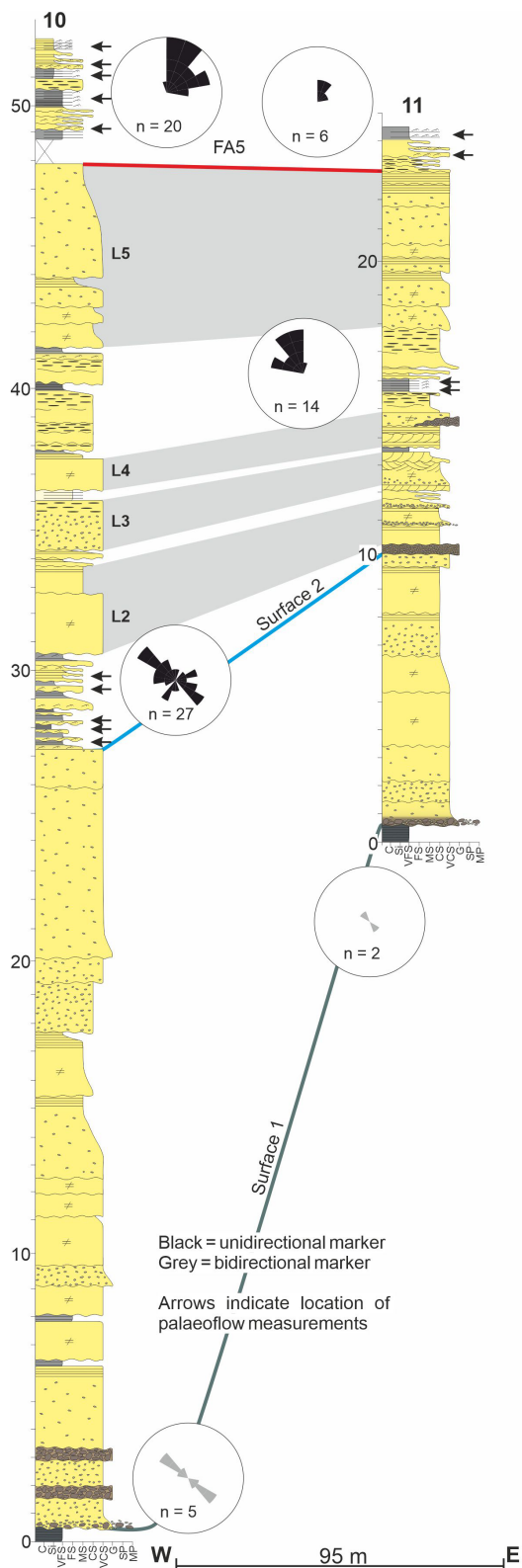
FIGURE 6 Correlation panel for the NSB, and associated palaeocurrent data. P4 and overlying stratigraphy is present in the NSB, but underlying stratigraphy cannot be correlated with the SSB. Log location shown in Figure 1D

Interpretation: The lateral variation in thickness and disaggregation is consistent with interpretation of FA1C as a slide (Milana et al., 2010; Valdez Buso et al., 2019) from remobilisation of a sandbody, with toewall buttressing resulting in imbricated thrusts. Previous authors named FA1C in the top of the studied succession as MTD 6 (Milana et al., 2010; Valdez Buso et al., 2019).

3.2 | Facies association 2: Axial channel-fill

3.2.1 | (A) Pebbly sandstones and conglomerates

Description: Laterally discontinuous beds (0.1–0.8 m thick) bounded by erosion surfaces overlie the deepest point of a composite erosion surface (>75 m of incision into FA1), vary markedly in thickness and facies. Beds vary in proportions of clast:matrix from clast to matrix -supported. Matrix-supported beds consist of poorly sorted, granule to cobble-size clasts with a wide range of rock types and shapes, from rounded to angular (Figure 3D), supported by a dark grey-brown, poorly sorted, medium to coarse-grained sandstone and white granule matrix. Clast-supported beds have a narrower range of clast sizes, from granule to large pebble-size, with a coarse-grained sandstone matrix. Grooves (0.1 m deep) are present on the base of matrix-supported beds.

Interpretation: Lenticular, clast-supported pebbly sandstones bounded by erosion surfaces are interpreted as lag deposits, with clasts carried as bedload transport (Mutti, 1992; Mutti & Normark, 1987). Poorly sorted, matrix-supported, clay-poor beds suggest deposition from debris flows (Mutti et al., 2003), with the presence of grooves further indicating passage of cohesive flows, such as debris flows or slumps (Baas et al., 2021; Peakall et al., 2020). The position of these lag deposits associated with the composite erosion surface supports the interpretation that FA2A formed through the passage of multiple erosive flows that formed a sediment bypass-dominated zone (Gardner et al., 2003; Mutti & Normark, 1987; Stevenson et al., 2015; Winn & Dott, 1977).

3.2.2 | (B) Amalgamated sandstone beds

Description: Homogeneous, erosively based sandstone beds (0.5–*ca* 4 m thick), with common amalgamation surfaces, comprising white-grey, angular to sub-angular, medium to well-sorted, very coarse-grained and granular

TABLE 1 Summary of facies associations in this study

Facies Assoc.	Lithology	Bed geometry	Basal surface	Sedimentary structures	Depositional process	
FA1A	Clast- to matrix-supported poorly sorted deposit with megaclasts	Up to 70 m thick	Stepped erosion surface	Clast-supported medium-grained sandstone clasts transitioning into matrix-supported gravel-pebble layers. Sheared margins to clasts	Debrite emplaced as a single event cutting into substrate (Dott, 1963; Moscardelli et al., 2006; Nardin et al., 1979)	Remobilised deposits
FA1B	Matrix-supported, siltstone-rich, poorly sorted deposit.	Up to 150 m thick.	Transitional with FA1A.	Rare pebbles and cobbles, gravel stringers. Siltstone matrix is folded and sheared.		
FA1C	Interbedded, sandstone-rich deformed deposit.	>7 m thick	Erosive	Clasts distributed throughout some sandstone layers, otherwise structureless	Slide emplaced through remobilisation of a sandbody, with toewall buttressing (Milana et al., 2010; Valdez Buso et al., 2019)	
FA2A	Pebbly sandstones and conglomerates.	0.1–0.8 m thick, laterally discontinuous.	Loaded or erosive with grooves.	Matrix-supported: rounded to angular, granule to cobble clasts. Clast-supported: granule to large pebble. Structureless.	Matrix-supported deposits from cohesive flows (debris flows or slumps; Peakall et al., 2020). Clast-supported lag deposits from bedload transport (Mutti & Normark, 1987).	Axial channel-fill
FA2B	Amalgamated sandstone	0.5–4 m thick	Erosive, rare flute casts	Structureless or weak normal grading and amalgamation. Rare siltstone clasts at bed bases	Rapid deposition from high-density, steady, uniform turbidity currents (Bouma, 1962; Kneller & Branney, 1995; Lowe, 1982)	
FA2C	Normally graded sandstone	0.3–2.5 m thick, varying laterally	Erosive	Structureless or normally graded sandstone with abrupt grain-size break to current ripple and planar laminated sandstone/ siltstone	High-density turbidite (Lowe, 1982), transitioning to low-density turbidite and reworking by dilute flows (Allen, 1984; Best & Bridge, 1992; Southard, 1991)	
FA3A	Fissile sandstone, siltstone thin beds	<2 cm to mm thick, laterally continuous	Sharp	No clear grain-size trends, sharp bed bases and tops. Microripples	Suspension fall-out from dilute upper part of rapidly waning turbidity currents (Lowe, 1988; Mantz, 1978; Rees, 1966)	Terrace deposits
FA3B	Scoured sandstone thin beds		Erosive	Dispersed clasts, concentrated in scours. Cross-ripple and parallel lamination. Normally graded beds	Deposition and tractional reworking by upper dilute parts of turbidity currents (Lowe, 1982)	

TABLE 1 (Continued)

Facies Assoc.	Lithology	Bed geometry	Basal surface	Sedimentary structures	Depositional process	
FA4A	Tabular sandstone beds	*ca* 1 m thick, tabular	Erosive (limited)	Weak normal grading, rare parallel and cross ripple lamination, and isolated siltstone clasts	High-density turbidite (Bouma, 1962; Lowe, 1982), reworking by dilute flows (Allen, 1984; Southard, 1991)	Lobe
FA4B	Sandstone-siltstone thin beds	1–30 cm thick, tabular	Erosive	Structureless sandstones, or exhibit weak planar and rare cross ripple lamination. Siltstones finely laminated and lack grading. Bed contacts are sharp or gradational	Turbidity current deposits. Sharp grain-size changes suggest density stratification (Kneller & McCaffrey, 1999) or bypass (Stevenson et al., 2015). Gradational contacts suggest trapping of turbidity currents (Sinclair & Tomasso, 2002)	
FA4C	Bipartite sandstone-siltstone clast-rich sandstone	0.3–0.8 m thick	Erosive	Lower sandstone structureless, with dispersed siltstone clasts. Upper division abundant siltstone clasts, variable size and geometry	Lower division high-density turbidite (Lowe, 1982; Talling et al., 2012), with overlying division interpreted as a genetically linked debrite, forming a hybrid bed (Haughton et al., 2003, 2009; Talling et al., 2004).	
FA5	Interbedded siltstones, and graded clast-rich sandstones	0.5–20 cm thick	Sharp or erosive	Micaceous, parallel-laminated siltstone and planar, current and climbing ripple sandstone with basal grooves, with clasts dispersed throughout	Deposition from, or reworking by rapidly decelerating, low-density turbidity currents (Talling et al., 2012; Jobe et al., 2012). Grooves on base of clast-rich sandstones indicate debris flows (Peakall et al., 2020)	Lobe fringe

sands (Figure 3E) that stack to form laterally extensive packages. Typically, beds are structureless with weak normal grading and planar lamination at bed tops. Bed bases occasionally exhibit large, wide flute casts and weakly stratified siltstone clast-rich units that form discrete layers, and some beds contain dish structures.

Interpretation: Thick, clean sandstones deposit under high-density turbidity currents and sandy debris flows (Bouma, 1962; Kneller & Branney, 1995; Lowe, 1982; Mutti, 1992; Talling et al., 2012). The alignment of siltstone clasts and presence of flute casts on the base suggests deposition from turbidity currents (Baas et al., 2021; Kneller & Branney, 1995; Peakall et al., 2020; Talling et al., 2012). Furthermore, flute geometry suggests deposition in a proximal environment (Peakall et al., 2020; Pett & Walker, 1971). Structureless sandstones within the succession can result from deposition from a steady, uniform current (Kneller & Branney, 1995), which may be sufficiently rapid to induce liquefaction (Kneller & Branney, 1995; Lowe, 1982; Peakall et al., 2020) precluding the development of depositional bedforms (Lowe, 1982).

3.2.3 | (C) Normally graded sandstone beds

Description: Beds with lateral thickness variations (0.3–2.5 m thick) have erosional bases, and comprise well-sorted, structureless, normally graded, white-grey, very coarse-grained sandstone, with granules dispersed throughout, and dish and flame structures. Commonly, there is an abrupt grain-size break to a fine-grained planar and ripple laminated sandstone and siltstone division (Figure 3F).

Interpretation: Very coarse-grained structureless sandstones were deposited by high-density, sand-rich turbidity currents (Lowe, 1982). Dewatering structures form through liquefaction (Mulder & Alexander, 2001; Stow & Johansson, 2002) probably related to rapid deposition (Lowe, 1982; Peakall et al., 2020). Finer-grained material was deposited from low-density turbidity currents, with tractional structures formed from reworking by dilute flows above the bed (Allen, 1984; Best & Bridge, 1992; Southard, 1991). The grain-size break is interpreted to reflect the transition from high to low-density turbidity current deposition (Sumner et al., 2008), and may indicate sediment bypass (Stevenson et al., 2015).

3.3 | Facies association 3: Terrace deposition

3.3.1 | (A) Fissile thin beds

Description: Primarily comprises relatively continuous fissile beds (<2 cm to millimetres thick) of siltstone to fine-grained sandstone (Figure 3G), with no clear lateral or stratigraphic bed thickness or grain-size trends (Figure 5B,C). Thicker beds exhibit asymmetric 'micro-ripple' lamination (<1 mm amplitude, *ca* 5 mm wavelength) on the upper surface of coarse-grained siltstones. Bed bases and tops are sharp, with little evidence of erosion into underlying beds.

Interpretation: Deposition from upper, dilute parts of turbidity currents (Lowe, 1988). Thin beds suggest low suspension fallout rates. The micro-ripples on the tops of beds are the product of very early stage (incipient) ripples in silts (Mantz, 1978; Rees, 1966), suggesting limited time for tractional reworking and thus a rapidly waning flow.

3.3.2 | (B) Scoured thin beds

Description: Undulating, fine to coarse-grained, well-sorted sandstone beds with erosive bases, which are commonly truncated by scour surfaces (Figure 3H). Thinner beds are normally graded, and thicker beds show little grain-size variation, with rare basal siltstone chips (0.5–1.5 cm diameter). Typically, beds of coarser grain size exhibit cross ripple lamination along with granules dispersed throughout beds that can follow ripple foresets, and finer-grained beds exhibit parallel lamination. Scour-fills are concentrated in granules, and contain siltstone clasts and rare inclined laminae sets.

Interpretation: Deposition and tractional reworking by upper dilute parts of turbidity currents (Lowe, 1982). The presence of abundant scour surfaces, infilled by granules indicates sediment bypass, and suggests deposition at a relatively low elevation with respect to the active channel (Hansen et al., 2015). Normal grading and tractional structures overlying these surfaces suggest formation by low-density turbidity currents (Kneller & Branney, 1995; Lowe, 1988).

3.4 | Facies association 4: Lobe environments

3.4.1 | (A) Tabular sandstone beds

Description: Metre-thick tabular beds with limited basal erosion comprised of white-grey, angular to sub-angular, medium to well-sorted, coarse-grained sandstone and granules. Beds are weakly normally graded, with rare parallel and current ripple laminations at bed tops and rare isolated siltstone clasts in bed bases. Bed contacts are amalgamated or separated by a defined erosion surface.

Interpretation: Normally graded sandstones are interpreted to form from high-density turbidity current

deposition (Bouma, 1962; Lowe, 1982; Talling et al., 2012), with tractional structures formed by reworking of the bed by dilute flows (Allen, 1984; Best & Bridge, 1992; Southard, 1991). Weak normal grading and planar lamination indicate deposition from a waning current (Kneller & Branney, 1995).

3.4.2 | (B) Sandstone-siltstone thin beds

Description: Beds (1–30 cm thick) comprise a basal dark yellow, medium-grained sandstone division and an overlying dark grey-black, fine-grained siltstone division (Figure 3I), with the siltstone often thicker than the sandstone. Sandstone divisions have erosional bases, are tabular, and commonly exhibit weak planar and rare current ripple lamination (Figure 3J). Typically, siltstone divisions are finely laminated, lack grading and are thicker than the underlying sandstone layer. Some beds exhibit a sharp grain-size change from sandstone to siltstone, with some normally graded from sandstone to siltstone within 2 cm.

Interpretation: Structureless sandstones suggest high-density turbidity currents. The nature of the contact between the sandstones and the overlying siltstones indicates two different processes. Beds with an abrupt transition from sandstone to siltstone division are interpreted as a function of density stratification within the flow (Kneller & McCaffrey, 1999), or as a result of bypassing of the transitional grain-size fraction (Stevenson et al., 2015). In contrast, beds with grading from sandstone to siltstone divisions suggest trapping of turbidity currents (Sinclair & Tomasso, 2002), which were unable to surmount a down-dip obstacle.

3.4.3 | (C) Bipartite beds

Description: Bipartite beds (0.3–0.8 m thick) comprise a lower, moderately well-sorted, coarse-grained to medium-grained sandstone division, and an upper poorly sorted silty-sandstone division (Figure 3K). The lower division is characterised by erosive bases and is structureless with siltstone rip-up clasts, dispersed throughout. The upper division is matrix-supported, poorly sorted silty–sandstone with dispersed medium and coarse sand grains, and siltstone clasts (0.1–6 cm diameter). Larger siltstone clasts are located in the lower bed division and are elongated, with sub-angular to rounded edges, whilst smaller clasts (<2 cm diameter) are dispersed throughout. The contact between divisions is diffuse.

Interpretation: The lower sandstone division is interpreted as a high-density turbidite (Lowe, 1982; Talling et al., 2012). The overlying silty-sandstone with clasts dispersed throughout, is interpreted as a debrite, which is genetically linked to the underlying turbidite, with the bipartite beds interpreted as hybrid beds (Haughton et al., 2003, 2009; Talling et al., 2004).

3.5 | Facies association 5: Lobe fringe deposits

Description: Beds (0.05–0.2 m thick) of sharp-based, dark red-brown to dirty yellow, well-sorted medium-grained sandstone with an abrupt transition to thick (up to 0.75 m, compared with 0.2 m sandstone) coarse-grained siltstone (Figure 3L). Sand grains are sub-rounded to rounded, and beds contain a high proportion of mica. Beds exhibit abundant planar, ripple and climbing ripple lamination. Normally graded sandstone beds are interbedded with coarse-grained siltstone beds (0.3–0.85 m thick packages), exhibiting parallel lamination and rare centimetre-scale medium to coarse-grained sandstones. The thickest exposure (Log 3, Figure 4) shows a coarsening and thickening-upward succession, passing from siltstones interbedded with centimetre-scale medium and coarse-grained sandstones, to medium-grained sandstone beds up to 0.2 m thick and thin siltstones. Rare sharp or erosively based siltstone clast-rich medium-grained sandstone beds (0.2–0.4 m) are present in the south-west, close to the boundary with FA1A. Clasts are disseminated throughout beds, with no evident stratification or grading, with bed bases occasionally exhibiting grooves. Rare, isolated wood fragments are found on bed contacts.

Interpretation: Tractional structures formed through deposition from, or reworking by, low-density turbidity currents (Talling et al., 2012), with climbing ripples indicating rapidly decelerating flows (Jobe et al., 2012). The abundant mica and the presence of wood suggest a direct terrestrial source, and in turn hyperpycnally driven flows (Zavala & Pan, 2018). Additionally, basal grooves suggest bypassing of debris flows (Peakall et al., 2020), and deposition of beds with chaotically distributed clasts and no grading is indicative of debrites (Talling et al., 2012).

4 | STRATIGRAPHIC FRAMEWORK, ARCHITECTURE AND DEPOSITIONAL ELEMENTS

The La Peña succession is subdivided into four units (Units 1–4), with Unit 2 further divided into four stratigraphic packages (only present in the SSB; Figure 4), based on lithology, facies, bed geometry and bounding surfaces.

4.1 | Unit 1—MTD 5

Unit 1 (*ca* 200 m thick) is MTD 5 of Milana et al. (2010) and Valdez Buso et al. (2019), and comprises *ca* 70 m of FA1A and *ca* 130 m of FA1B, with an erosional base (Figures 2A and 3A). Megaclasts decrease in size and number upwards into the matrix-supported upper part of MTD 5 (Figures 1C and 3A).

4.2 | Surface 1 (S1)—basal composite erosion surface

In the SSB area, MTD 5 is cut by a >75 m deep, 400 m wide concave-up surface, with stepped margins to the south-west and north-east (Figure 4). The south-west margin steepens with height (maximum 70°) and exhibits an uneven geometry, before passing westwards to an irregular surface that flattens to sub-horizontal (Figures 1 and 4). This surface is also characterised by sand injection into underlying MTD 5. The north-east margin is faulted (Figures 1 and 2A), with the exposure of S1 on the uplifted block sub-horizontal (Figure 2B,C); the lower portion of this margin is inferred to be a similar gradient to the south-west margin. Surface 1 in the NSB area is characterised by smooth margins (to the west and north-east). The west margin is steeper and faulted, and the north-east margin is more rugose (Figure 2C). Grooves and other tool marks are present on S1, with depths of up to 0.15 m and a greater width than depth. Palaeoflow from grooves in S1 range from 130/310° to 174/354° in SSB, and from 108/288° to 143/323° in NSB. Pebbles are occasionally present in the base of the tool, suggesting they were the tool-makers. These grooves were probably cut by bypassing flows with cohesive strength such as debris flows, or the debritic component of hybrid beds (Baas et al., 2021; Peakall et al., 2020). Immediately overlying S1 are the lenticular conglomeratic beds of FA2A, interpreted as lag deposits, present on the stepped surfaces and the lowest point of S1. The stepped geometry, and indication of sediment bypass at different stratigraphic levels, suggest Surface 1 is a composite erosion surface that deepened through time (cf. Hodgson et al., 2016; Hubbard et al., 2014).

4.3 | Unit 2—SSB area

4.3.1 | Package 1 (P1)—bypass lags and amalgamated axial channel-fills

Package 1 (P1; *ca* 20 m thick) directly overlies the lowermost part of S1 in the SSB (Figure 4) and comprises a laterally discontinuous basal conglomerate (up to 3 m thick; FA2A), with overlying tabular, commonly amalgamated, very coarse-grained sandstone beds (*ca* 17 m thick; FA2b). Multiple erosion surfaces separate FA2A and FA2B, suggesting a sediment bypass-dominated period. FA2B is present up to the first step in S1 to the south-west, where beds onlap S1 at an angle of *ca* 20°. Flute casts on the base of a P1 bed indicate palaeoflow ranges from 265–040°, but predominantly to the north-west (Figure 4). Towards the top of P1, a thin (0.2 m thick) partially preserved unit of ripple laminated fine-grained sandstones (palaeoflow range 140–040°) and coarse-grained siltstones is interpreted to represent a period of reduced sediment supply. The sand-rich, commonly amalgamated deposition from high-energy flows, and location within an incisional confining surface (S1) supports interpretation of these deposits as axial channel-fills.

4.3.2 | Package 2 (P2)—channel aggradation

In general, Package 2 has a higher proportion of fine-grained material, siltstone clasts and thinner beds than P1. FA2C dominates P2, and thickens from 3 m in the east to 16.5 m above the deepest point of S1, then thins to 6 m in the south-west (Figure 4). P2 is subdivided into lower and upper subunits based on the geometry and lateral extent of beds (Figure 4). Lower P2 is characterised by southward-thinning beds (from *ca* 9 to 2.5 m thick) extending across the channel cut; to the east, the base of lower P2 directly overlies S1 (Figure 2B,D) and further west it overlies Unit 1 (Figures 2B and 4). Lower P2 is correlated with the sandstone exposure on top of the horst block to the north (Figures 2B and 4). This exposure of P2 can be traced northwards across the horst block (Figure 2C) and correlated with an erosion surface overlying confined heterolithic deposits (T1) in the north (Figure 1). The base of P2 in contact with S1 and Unit 1 indicates the presence of a palaeohigh during deposition, or a stepped geometry of the north-east margin above the level of P1 deposition. Groove data from S1 on the horst block give palaeoflow readings of 092/272°-172/352°. Above this, lower P2 thins westward from *ca* 9 to 2.5 m thick, whilst on the eastward side it is cut by the basal surface of P3 (Figure 4). Upper P2 exhibits multiple concave-up erosion surfaces bounding laterally discontinuous bodies of sandstone-rich deposits (FA2C; Figure 4), interpreted as smaller-scale channel-fills.

The thickest part of upper P2 in the west comprises lenticular beds with erosion surfaces defining channelised bodies (1.5–4 m thick). These exhibit a highly aggradational stacking pattern, with limited lateral offset to the east (Figure 4). Palaeocurrent measurements taken from ripple cross laminations in finer-grained bed caps have a

wide range of directions (062–326°) (Figure 4), most probably indicating flow deflection from surrounding topography (Kneller et al., 1991).

4.3.3 | Package 3 (P3)—channel widening

The base of Package 3 is erosional, and is coincident with a prominent step in Surface 1 on the south-west margin, marking widening of the SSB (Figure 4). Because pebbly sands and conglomerates (FA2A) are only present overlying S1 on the step, and not associated with P3 within the channel cut, the step is interpreted to have formed during the initial formation of S1. P3 is *ca* 11 m thick and comprises the same tabular, amalgamated sandstone facies (FA2B) as P1, with no fine-grained bed caps (Figure 4). It is not possible to identify the lateral and vertical extent of P3 in the SW of the SSB, due to exposure limitations. However, bed thickness, degree of amalgamation, and lack of fine-grained material suggest that flows were still channelised at this point.

4.3.4 | Package 4 (P4)—transition from confined to weakly confined

Package 4 is the most laterally extensive in the La Peña area, and is present in the SSB and NSB (Figures 1 and 4). The base of P4 is characterised by an irregular erosion surface (Surface 2 (S2)), overlying P3, and off-axis deposition to the south-west (Figure 4). S2 incises up to 2 m in the east, but the geometry to the south-west is unknown, due to exposure limitations. In Log 4, the S2 surface is marked by a scour infilled with mud-clast-rich FA2A, indicating the passage of, and deposition from, debris flows (Peakall et al., 2020). P4 (*ca* 22.5 m thick) coarsens and thickens upwards (Figure 5), and comprises five distinct, laterally variable but tabular sandstone beds and bedsets of FA4A (herein named L1-5), intercalated with packages of thin-bedded sandstones and siltstones (FA4B). The upper stratigraphy is characterised by hybrid beds (FA4C), which are commonly found in distal lobe fringes (Hodgson, 2009; Spychala et al., 2017a, 2017b), although hybrid beds are also observed in proximal environments, where the debritic component may be sand-rich (Brooks et al., 2018; Fonnesu et al., 2015). L1-L5 are dominated by a thick sandstone bed, and in the case of L1 and L5, amalgamated sandstones (Figures 4 and 5). Together with the overlying thinner beds, these are interpreted as lobe elements, collectively forming a single lobe (*sensu* Prélat et al., 2009) confined within S1, marking an abrupt stratigraphic change from channelised to lobe deposition.

In the lower stratigraphy of P4, ripple current lamination record palaeocurrents ranging from 134 to 352°, and together with the pronounced normal grading of beds from sand to silt, suggests flow deflection off, and trapping of flow by, topography downstream (Hodgson & Haughton, 2004; Sinclair & Tomasso, 2002). L1 and S2 are cut by a high angle (*ca* 45°) erosion surface (Figure 5) overlain by *ca* 3.5 m of interbedded sandstones (0.1–0.5 m thick), which is interpreted as a scour-fill (Figure 4).

L4 is continuous across the outcrop and amalgamates with L3 eastwards (Figures 1, 4 and 5). In the central SSB area and westward, L3 and L4 are separated by a package of hybrid beds, reaching a maximum thickness of 5 m. L3 and L4 onlap the western margin (Figure 1). The upper part of P4 comprises a laterally continuous package of hybrid beds (4 m thick), overlain by L5 (*ca* 3–7 m thick). Palaeocurrents within the lower package of hybrid beds range from 026–332° and show a 360° range across package P4 (Figure 4), further supporting the role of flow deflection and reflection in the upper package of hybrid beds.

4.4 | Unit 3—Overlying turbidites (FA5)

Unit 3 is correlated from the SSB to the NSB to form a high aspect ratio package (Figure 1). The contact between Unit 2 and Unit 3 (FA5) is characterised by an abrupt transition from thick-bedded and amalgamated coarse-grained sandstones (L5) to coarse-grained siltstones (Figure 4). Unit 3 forms a 2–5 m thick coarsening and thickening-upward package from siltstones interbedded with centimetre-scale sandstones to increasingly thick (up to 10 cm) sandstone beds (Figure 4). Palaeocurrents from current ripple lamination range from 020 to 080°NE, with grooves averaging 080°–260°. Commonly, thin-bedded, rippled sandstones in tabular packages are interpreted as lobe fringe deposits (Marini et al., 2016; Prélat et al., 2009; Spychala et al., 2017a). The absence of hybrid beds suggests flows did not transform because they were not able to entrain a muddy substrate. The thickening upwards supports a transition from distal lobe fringe to lobe fringe, and progradation of the system.

4.5 | Unit 4—MTD 6

Unit 3 is overlain by MTD 6 (up to 7 m thick; Figures 1 and 3C) in both the SSB and the NSB, transitioning from massive sandstone beds, to an imbricated thrust complex with pop-up sand blocks in the north-east of the NSB. Previous authors used the orientation of thrust faults

within the MTD to determine a palaeoflow to the north-east (Sobiesiak et al., 2017).

4.6 | NSB fill

The NSB fill is up to 60 m thick (Figure 6), with 2 m of len-ticular, conglomeratic beds (FA2A) overlying S1. Above this, *ca* 40 m of very coarse-grained sandstones (0.4 to *ca* 3 m thick; FA2B) is present that thin and become less amalgamated towards the margins. The presence of high-density turbidity current deposits confined by S1 supports an interpretation of axial channel sandstones. Above this, S2 is overlain by a 0.2 m thick, laterally discontinuous bed of FA2A in the east (Figure 6). P4 (L2-L5) of Unit 2 is cor-related from the SSB, with Units 3 and 4 also present over-lying the NSB. P4 has a similar stacking pattern, with four distinct sandstone beds (FA4A) intercalated with FA4B and FA4C. FA4B is present in the central part of the out-crop, with a 360° spread of palaeocurrents, but absent to the north-east. L2 to L4 are tentatively correlated across the area. L5 and Unit 3 were walked out and correlated across faults using their distinctive lithology and bed ar-chitecture. Unit 3 (*ca* 3 m thick) contains palaeocurrents ranging from 357°-084°. Overall, P4 thins and onlaps to-wards the north-east margin of MTD 5, before passing into the subcrop (Figure 1).

4.7 | Off-axis deposition on elevated surfaces

Three distinct sedimentary successions overlie steps in Surface 1, with one between the NSB and SSB (T1) (Figure 1) and the others on small (10 m wide) concave-up steps (T2 and T3) to the west of the SSB (Figures 1 and 4). These deposits share similar depositional architectures and processes.

4.7.1 | Terrace deposits 1 (T1)

T1 is located between the SSB and NSB, and directly over-lies S1 and MTD 5, (Figures 1 and 7A,B,C). T1 (*ca* 15 m thick) primarily comprises fissile thin beds (FA3A), with rare 0.05–0.1 m thin beds (FA3B) exhibiting minor ero-sional bases (Figure 7B,C). Palaeocurrent measurements from current ripple lamination range from 040 to 340°. Deformation and dip of T1 deposits towards the south-west indicates post-depositional rotation and sliding towards the axis of the NSB (Figure 7A). The rotated and deformed T1 deposits are cut by a SSW-NNE orientated erosion surface (*ca* 20° dip) (Figure 7A), overlain by a 0.75–1.2 m

thick sandstone bed (FA2B). Grooves on the base of the sandstone (palaeoflow range 070/260°–100/280°) indicate passage of debris flows or other strongly cohesive flows over the surface (Peakall et al., 2020). This sandstone bed can be traced laterally to the west across the horst block, where it overlies MTD 5, and is correlated across a fault, to the base of P2 in the SSB outcrop (Figures 1 and 2A,B,C). This indicates that the deposition, deformation, and ero-sion of T1 occurred prior to the deposition of P2 within the SSB.

4.7.2 | Terrace deposits 2 (T2)

T2 (24 m thick; Figures 1 and 4) is located to the south-west of the SSB, and is underlain by a package of con-glomerates and pebbly sandstones (FA2A) that overlie S1, and are interpreted as deposits from a sediment bypass-dominated phase. T2 comprises two discrete sections; the lower section (*ca* 5 m thick) comprises 0.1–0.8 m thick packages of scoured thin beds (FA3B), and the upper sec-tion (*ca* 3 m thick) comprises fissile thin beds (FA3A). T2 is cut by S2 (Figure 4).

4.7.3 | Terrace deposits 3 (T3)

T3 is the thickest deposit of this type (*ca* 32 m; Figures 4, 7 and 8). The lower part of T3 overlies a package of peb-bly sandstones and conglomerates (FA2A, 0.4–0.8 m thick) that overlie S1, which are interpreted as bypass-dominated deposits. The overlying T3 stratigraphy is subdivided into a lower and upper succession (Figure 8). Lower T3 com-prises six 1–3 m thick coarsening and thickening-upward units (T3.1–3.6) of fissile (FA3A; Figure 7D) and scoured thin beds (FA3B). The lowermost unit (T3.1) (Figure 8) coarsens upwards from coarse-grained, micro-rippled silt-stone (palaeocurrents *ca* 170°) (FA3A, >1 cm thick; Figure 7E) to ripple laminated coarse-grained sandstone (palaeo-currents throughout, range from 010–335°, a 325° spread) (FA3B, *ca* 4 cm thick; Figures 7F and 8). The overlying unit (T3.2; *ca* 2.5 m thick, Figure 8) is characterised by multiple centimetre-deep scour surfaces that are orientated broadly W-E/NW-SE (090/270°-140/320°) and mantled with gran-ules (Figure 7F). The scour-fills comprise a matrix of medium-grained sandstone, with siltstone chips concen-trated close to the scour surface, but dispersed throughout. Scours are 3–5 cm in length (Figure 7F), and exhibit rela-tively smooth bases, and a constant longitudinal maximum depth. Palaeocurrent measurements from current ripple lamination throughout T3.2 range from 030 to 358° (a 328° spread). T3.3 (*ca* 1.5 m thick) comprises coarse-grained sandstones (FA3B) with erosional bases, interbedded with

planar laminated coarse-grained siltstones (FA3A) with abundant current ripple lamination (palaeoflow 070–352°, a 282° spread) and grooves (palaeoflow 098/278°, 138/318°). The next 3 units (T3.4–T3.6) are characterised by coarse-grained planar laminated siltstone beds, interbedded with granule-rich sandstones (Figure 8) that are current ripple laminated in T3.4 (palaeocurrent 040–110°, a 70° spread). Above this, sandstone beds thicken above deeper erosion surfaces, and contain abundant siltstone clasts distributed throughout. In summary, the scours and grooves are orientated approximately W-E to NW-SE, whilst the ripples show an almost 360° range of palaeocurrents (Figure 4).

The base of Upper T3 is marked by a 20 cm thick granule-rich, very coarse-grained sandstone with an erosional base overlain by abundant siltstone clasts (Figure 8). Six overlying beds (0.14–1.16 m thick) are normally graded from very coarse to fine-grained sandstone or coarse-grained siltstone with parallel lamination. This interval is overlain by a distinctive bed containing convex-upwards, low-angle lamination, inclined towards the main conduit (Figure 7E), which resembles hummocky-cross stratification. Similar features have been documented by previous authors in turbidite systems, and in combination with palaeocurrent data are interpreted to form through deposition and reworking of reflected dilute flows (Hofstra et al., 2018; Mulder et al., 2009; Tinterri, 2011; Tinterri & Muzzi Magalhaes, 2011) forming a combined flow bedform. This is followed by six erosively based normally graded and locally planar laminated sandstone beds, then a sandstone-dominated interval with multiple erosion surfaces mantled by siltstone clasts. This succession is cut by a surface overlain by extra-basinal and intra-basinal small pebbles to large cobbles (up to 30 cm diameter) (Figure 8). Overlying beds form fining-upward packages of normally graded coarse to fine-grained sandstones, before the deposition of P4.

The elevated location of T1, T2 and T3 above the main conduit, the absence of physical bed-scale connections with axial deposits, the highly variable palaeocurrents (ripples with a full 360° range) and hummock-like bedforms indicating flow interactions, the distinctive thin beds with multiple scours mantled with granules, and the absence of wedge-shaped stratigraphy or downlap, support the interpretation of these successions as terrace deposits (Hansen et al., 2015, 2017a, 2017b; McArthur et al., 2019) with phases of sediment bypass, rather than internal levees (Kane & Hodgson, 2011) or channel margin deposits (Hubbard et al., 2014).

4.8 | Regional correlation

The La Charca outcrop (*ca* 2 km up-dip from La Peña) is *ca* 50 m thick (Figure 2E,F), and exhibits a stepped basal surface that cuts into MTC 5, overlain by sandstone-prone deposits similar to FA2A, which are in turn overlain by laterally thinning and/or amalgamated sandstone beds (<1 to *ca* 10 m thick) similar to FA2B (Figure 2F). The lack of stratigraphic information in the 2 km between the La Peña and La Charca outcrops means it is not possible to determine their exact relationship. However, their same stratigraphic position bounded by MTD 5 and MTD 6 (Figure 2E,F), and similar fill and geometry suggest some degree of connection between the two. The stepped basal surface and overlying sandstone-prone succession similar to FA2A supports a channelised setting with basal lag deposits, with laterally discontinuous sandstones above interpreted as stacked individual channel bodies.

5 | DISCUSSION

5.1 | Stratigraphic evolution

5.1.1 | Formation of S1

The stepped geometry, and pebbly sandstones and conglomerates (FA2A) overlying S1 at the base of P1 and on the south-west margin under P3 in the SSB, under the lowermost package of the NSB, and underlying T2 and T3 on elevated surfaces suggests that S1 deepened through multiple phases of erosion and sediment bypass. The south-west expression of S1 in the SSB is characterised by onlap and localised erosion, indicating limited modification of S1 and MTD 5 during P1. This supports the formation of the composite S1 during an initial downcutting phase dominated by sediment bypass (Hodgson et al., 2016; Hubbard et al., 2014), rather than reworking during aggradation. The ability of MTD 5 to support the formation of S1 suggests a high yield strength and cohesion.

These channel-fills with their ribbon-like low aspect ratio incision surfaces contrast markedly with the upper surface, and overlying depositional architecture, documented above thick MTDs in the Paganzo Basin at Cerro Bola >70 km to the north (Dykstra et al., 2011; Fallgatter et al., 2017; Sobiesiak et al., 2016). The Cerro Bola MTDs have tens of metres of relief, but the overlying deposits comprise several metres thick high aspect ratio megabeds without evidence for basal erosion. In the absence of clear truncation and evidence for sediment bypass as observed at La Peña, the depositional relief at Cerro Bola has been interpreted to be accentuated by post-depositional creep and/or compaction processes (Dykstra et al., 2011; Fallgatter et al., 2017; Kneller et al., 2016).
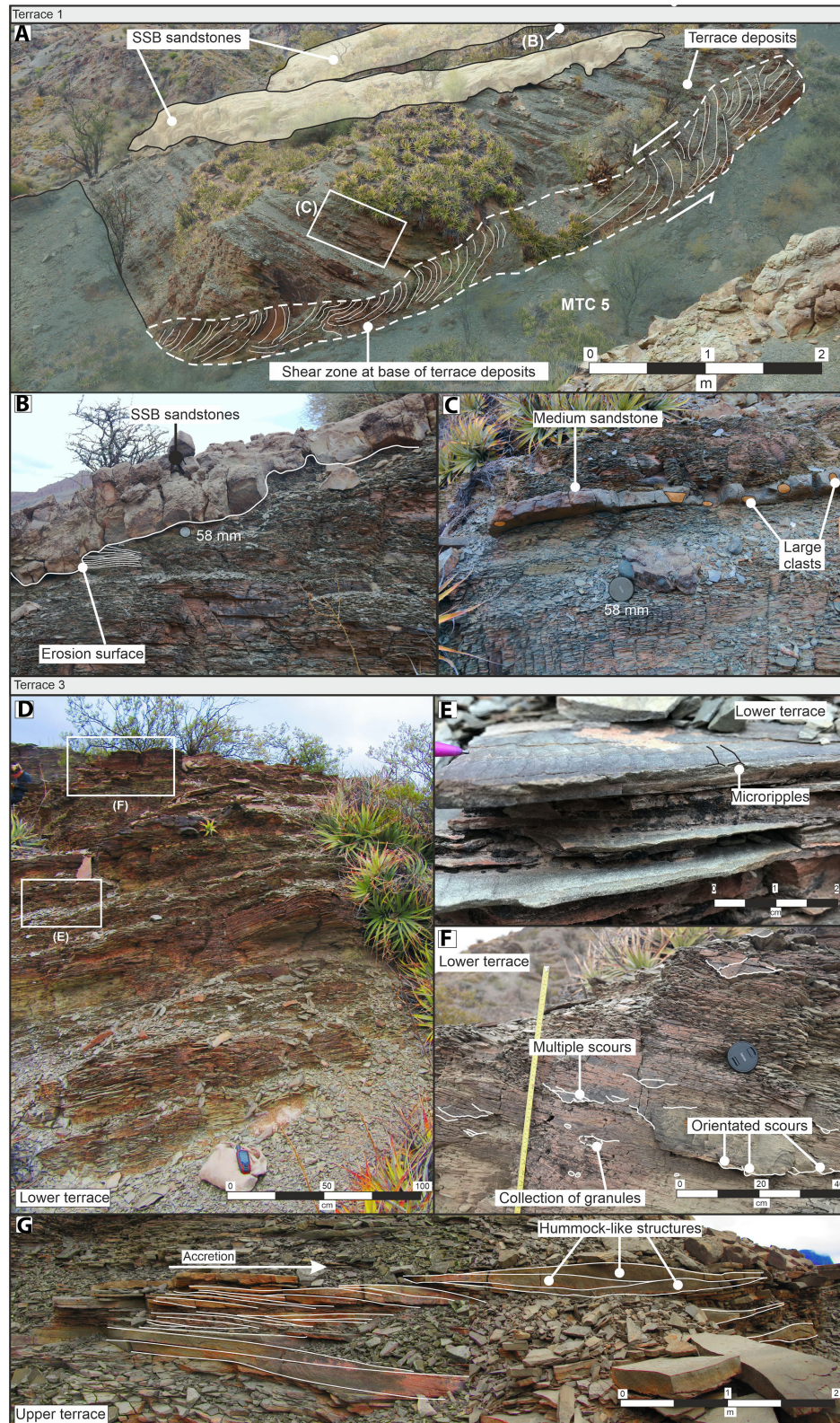
FIGURE 7 Examples of terrace deposits in the La Peña section. (A) Outcrop of Terrace T1, showing slip surface, and over-spilling channel sand eroding the terrace deposition. (B) Closer image showing the erosion of channel sand, and the predominantly thin-bedded nature of the terrace. (C) Medium-coarse-grained sandstone layer containing large clasts that are present throughout the terrace. (D) Lower section of Terrace T3. (E) Micro-ripples on thin beds in Lower Terrace. (F) Outcrop of the lower section of Terrace T3, showing predominantly scoured thin-bedded deposition. (G) Upper section of Terrace T3, characterised by increased bed thicknesses, with beds exhibiting lateral accretion, and hummock-like geometries
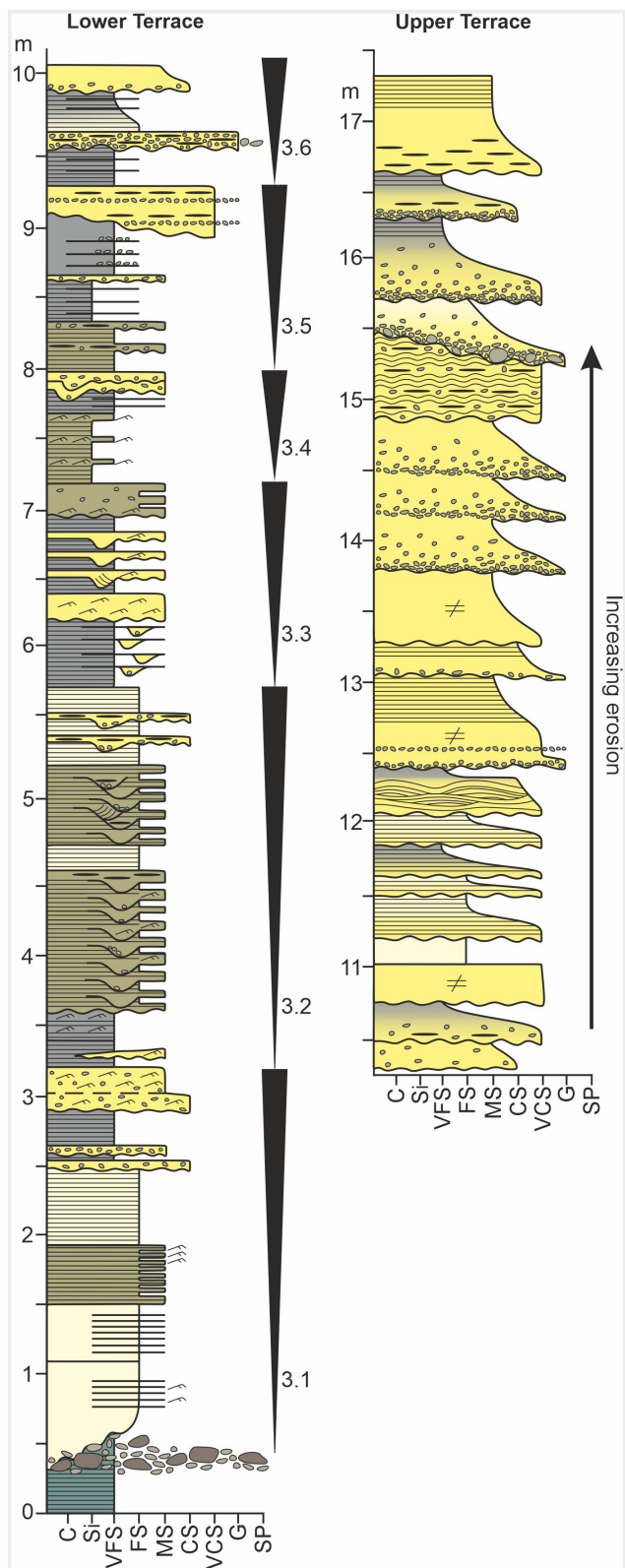
FIGURE 8 Sedimentary log through the lower and upper sections of Terrace T3, showing change in grain size, bed thickness and bed geometries. The lower section of the terrace is characterised by six packages of thickening and coarsening up beds. In contrast, the upper terrace is characterised by a lack of discernible bed thickness and grain-size trends but exhibits a higher degree of erosion and greater bed thicknesses

5.1.2 | Channelised deposition (P1–P3)

P1 represents the first stage of fill within the SSB, and is characterised by coarse-grained amalgamated sandstones above the lowest part of the S1 surface (Figure 9A). Overlying this, P2 is characterised by a wider grain-size range, fine-grained bed caps, and smaller-scale channelised bodies (Figure 9B). During P2, flows eroded into the remobilised terrace deposit T1, and were able to deposit either side of the palaeohigh between the SSB and the NSB. The increase in fine-grained material could either reflect a change in sediment source character, or a change in flow parameters resulting in reduced flow velocity and potential to bypass that affected grain-size sequestration along a system. The increase in finer material allowed formation and stabilisation of channels banks within the larger-scale conduit bounded by S1 (Peakall et al., 2007). The change in bed geometry may also reflect reduced confinement leading to lower local velocities and deposition and preservation of finer grain sizes, allowing elementary channels to form and migrate (Figures 4 and 9B). P3 is marked by tabular sandstone beds (Figure 9C), with the greater bed thickness, coarser grain size and level of amalgamation suggesting deposition from larger, higher energy flows, capable of bypassing finer-grained sediment down-dip (Kneller & Branney, 1995). There is no evidence for flow ponding, such as thick normally graded bed caps or a wide range of palaeoflow measurements to support flow reflection in P1-3.

5.1.3 | Down-dip confinement

S2, an irregular and laterally extensive erosion surface, cuts into P3 and T2 in both the SSB and the NSB, supporting an erosion and bypass-dominated phase that resculpted both the SSB and NSB systems (Figures 1, 4 and 5). This surface is overlain by a marked change to 6 m of interbedded FA4B (Figures 5 and 9D), which based on normally graded beds with fine-grained caps, are interpreted as deposits of fully or partially confined flows (Sinclair & Tomasso, 2002). This abrupt change suggests the presence of down-dip confinement of the channel system and formation of lobes. Complex palaeocurrents, ranging from 134–352° within this lower section further support the presence of down-dip confinement, with flow deflection and reflection off topography able to produce fully reversed measurements within a single deposit. The abrupt change from P3 to P4 is attributed to local changes within the system. Possible mechanisms include: (1) lateral collapse of the unstable MTD wall after formation of S2 and down-dip plugging of the conduit; (2) the infilling of down-dip accommodation on top of the MTD through

emplacement of an MTD; or (3) through continued deformation or (differential) compaction of the MTD impacting sediment transport pathways (Kneller et al., 2016; Tek et al., 2020; Zhao et al., 2019). The weak normal grading of L1 suggests that the scale of frontal flow confinement was limited, with fine-grained material transported further down-dip, and that the frontal confinement of lower P4 was related to emplacement of a minor MTD, possibly similar in scale to MTD 6. Evidence for flow confinement decreases up stratigraphy, although complex palaeocurrent indicators suggest some topography remained.

5.2 | Lobe progradation

P4 marks an abrupt change from channelised to lobe deposition. The extent of S2 to the north-east of the NSB is unknown. However, the near-consistent bed thicknesses of L1-L4 suggest a lack of lateral compensational stacking, and therefore some confinement by S2 and that lobe development shows flow size was scalable to the size of S2. Examples of lobate deposits underlying a channel system in unconfined settings are well-documented (Gardner et al., 2003; Hodgson et al., 2011, 2016; Macdonald et al., 2011), and lobes overlying individual channel complexes are associated with the 'spill' phase of channel development (Eschard et al., 2003; Gardner et al., 2003), and are unconfined. Lobes within the same confining surface as axial fill are undocumented, but semi-confined lobes have been documented in canyon settings in the South China Sea (Wu et al., 2018) and offshore Egypt (Morris et al., 2014).

Hybrid beds within channel confinement are rare, but have been documented in slope channel-fill of the Schiehallion Field (offshore the Shetland Islands), interpreted as a sign of system back-stepping or knickpoint migration (Haughton et al., 2009). Hybrid beds are more commonly associated with unconfined proximal (Brooks et al., 2018; Fonnesu et al., 2015), or lateral and frontal lobe fringe deposition (Haughton et al., 2003, 2009; Hodgson, 2009; Kane & Pontén, 2012; Spychala et al., 2017a, 2017b). Several mechanisms may result in hybrid bed deposition within the La Peña channel system, including: (1) system progradation where flow size remains the same, but as deposition was taking place in the upper portions of the channel cut, the conduit had sufficient width to allow 'unconfined' deposition from flows; (2) a reduction in flow size, resulting in underfit flows in relation to channel size forming 'unconfined' deposition (of hybrid beds); and (3) back-stepping of lobe complexes into the channel cut.

The thin-bedded sandstone-siltstone couplets (FA4B) in the lower section of P4 are interpreted as ponding of distal lobe fringe deposits, with increasing bed thickness
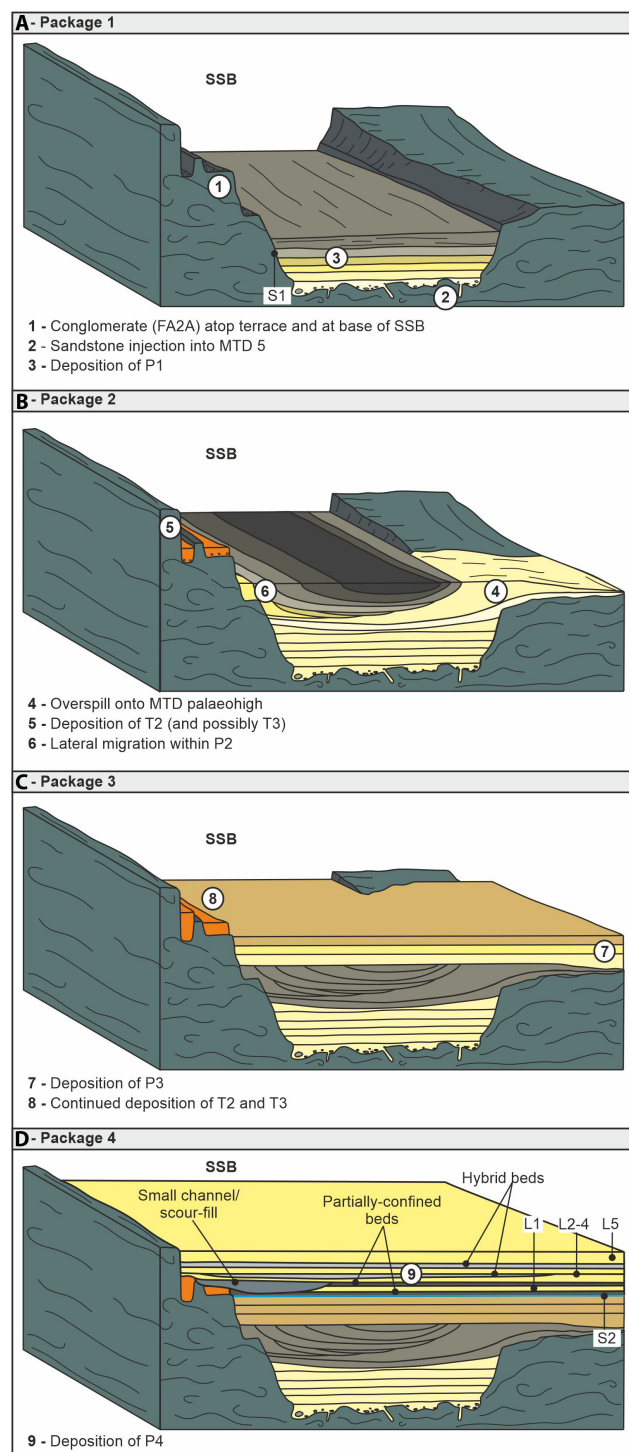

A - Package 1

1 - Conglomerate (FA2A) atop terrace and at base of SSB
2 - Sandstone injection into MTD 5
3 - Deposition of P1

B - Package 2

4 - Overspill onto MTD palaeohigh
5 - Deposition of T2 (and possibly T3)
6 - Lateral migration within P2

C - Package 3

7 - Deposition of P3
8 - Continued deposition of T2 and T3

D - Package 4

9 - Deposition of P4

FIGURE 9 Stratigraphic evolution of the La Peña section. (A) Deposition of Package 1 and Terrace 1 is followed by (B) overspilling onto an MTD palaeohigh, and partial erosion of Terrace 1 by the base of Package 2, before the initiation of channelised bodies, and concurrent lateral migration. Development of Terrace 2 and possibly Terrace 3. (C) Package 3 is characterised by a return to deposition of tabular geometries, and further development of Terrace 2 and 3. (D) The start of Package 4 deposition is characterised by repeated deposition of ponded and lobate beds, and erosion of these features by a small channel to the west. This is followed by repeated deposition of lobe and hybrid beds

and amalgamation of beds L1-L4, and decreasing volumes of fine-grained material suggesting progradation of a lobe complex. Erosional features in the lower portions of a lobe, such as the surface that truncates L1, are typically erosive products of larger flows (Figure 4), which suggests sufficient space within S1 to allow 'unconfined' deposition at this point. Sand-rich hybrid beds similar to those seen in La Peña have been observed in areas proximal to the lobe axis (Brooks et al., 2018; Fonnesu et al., 2015). A similar configuration is supported by deposition of L5, which is characterised by amalgamated sandstone beds indicating a lobe axis.

5.3 | Avulsion, lobe switching and back-stepping

The contact between package 4 of Unit 2 and the overlying Unit 3 is a sharp transition from axial lobe to distal fringe deposition, indicating a sudden change within the system. This corresponds with a change in palaeocurrent direction from the north-west to the north-east. The most probable mechanism for rapid abandonment of a lobe is upstream avulsion, leading to lobe switching (Macdonald et al., 2011; Prélat et al., 2010). As underlying bed geometries suggest lateral compensational stacking is not possible, it is probable that this new lobe back-stepped relative to the L1-L5 lobe, and Unit 3 represents distal lobe fringe deposition of a new lobe.

5.4 | Terrace development

Multiple mechanisms can form terraced surfaces within submarine channel systems (Hansen et al., 2015), which then act as sites for subsequent deposition. The presence of pebbly sandstones and conglomerates (FA2A) overlying S1 and immediately below T2 and T3 suggest that these surfaces were once the location of much higher energy and coarser-grained flows that mainly bypassed sediment basinward, compared to the overlying deposits. This, coupled with S1 cutting down 10 m over a width of 18 m (a gradient of *ca* 55°), and this elevation difference between T3 and the SSB (Figure 4) suggests formation of the terraced surface was through bend cut-off by entrenchment (Hansen et al., 2015), with T3 deposited in the older elevated and abandoned channel cut. The spread in palaeocurrent data in lower T3 (Figure 4) is indicative of flow deflection from frontal topography, with a large number of upstream flow indicators. Thus, plugging of the bend cut-off probably occurred through deposition at the 'exit' of the cut-off, possibly through reduced discharge and energy conditions within the abandoned channel

that caused trapping of suspended sediment (Constantine et al., 2010; Fisk, 1947; Toonen et al., 2012). An intermediary MTD high does not separate T1 and T2 from the main conduit, so the stepped surfaces these deposits are located on are probably entrenchment terrace surfaces (Babonneau et al., 2002, 2004; Hansen et al., 2015). The location of T1 adjacent to the NSB, and relationship with the base of P2, suggest T1 deposits were sourced from flows in the NSB, with flow deflection producing the dispersed palaeocurrent readings. Erosional terrace surfaces observed in the Indus and Benin-Major channel systems are interpreted to form during incision of the erosional fairway (Deptuck et al., 2003). Deposition on a terrace surface is governed by the thickness of a density-stratified turbidity current, and height of the terrace surface above the channel base (Hansen et al., 2015; Hansen et al., 2017a, 2017b). Consequently, assuming flow properties remain constant with time, increased height of terraces above the channel thalweg results in finer and thinner deposits (Babonneau et al., 2004, 2010). Thinning and fining-upward trends in external levees and terrace deposits have been attributed to increased flow confinement (Hansen et al., 2015; Hiscott et al., 1997; Kane & Hodgson, 2011; Normark et al., 1997). Thickening-upward and coarsening-upward trends have been interpreted to record system progradation of submarine fans (Hiscott, 1981; Mutti, 1984; Mutti & Ricci Lucci, 1972; Pickering et al., 1989) or lateral migration of a channel (Kane & Hodgson, 2011).

The thickest terrace succession (T3) exhibits two distinct styles of sedimentation separated by an abrupt change (Figures 7D through G and 8). The lower portion (T3.1-T3.6) is finer-grained, and dominated by thin beds (Figures 7D,E and 8), which form six thickening-upward packages (Figure 8), suggesting formation by stripping of upper parts of flows in the channel axis of the SSB, and of either repeated aggradation of the channel, and/or cyclical external controls on flow magnitudes. The presence of scour surfaces mantled with coarse grains within the terrace deposits (Figures 3H, 7F and 8) suggests that periodically there were more energetic, larger magnitude flows, or that periods of channel aggradation reduced the terrace height relative to the axis. Bed thickness, grain size, and numbers of granule and siltstone chip-rich intervals increase upwards in the upper T3 succession (Figure 8). This change could record: (a) higher aggradation of channel-axis deposits relative to terrace deposition, allowing increasingly coarse grain sizes and deposition of thicker beds, or (b) increasing flow magnitude through time, possibly through system progradation, or (c) some combination of the two. The overall pronounced coarsening-up succession of T3 suggests that the terrace deposits may largely reflect bed thalweg aggradation, rather than increasing flow magnitudes. Given that turbidity current

velocity decreases exponentially with height, once above the height of the velocity maximum, then even large increases in flow magnitude are unlikely to be able to produce major scour surfaces and deposition of granules and siltstone chips (up to 1.5 cm in size) on highly elevated terraces (*sensu* Babonneau et al., 2004). Given the overall bed stacking with repeated minor coarsening-up cycles, the lower part of the terrace is most easily explained as recording successive phases of channel thalweg aggradation during the infill phase. If related to initial downcutting and formation of S1, then there would need to be six progressively larger phases of bed aggradation within the channel, followed by renewed downcutting. The abrupt change between the deposits of the lower and higher terrace suggests that there was a major phase of channel aggradation at this point, which may have been accompanied by increased flow size.

5.5 | Relative timing of the SSB and NSB fill

Faulting in the centre of the study area largely prevents tracing of stratigraphic surfaces between the SSB and the NSB. The relationship between P2 and T1 provides the oldest observational constraints available of the temporal evolution of SSB and NSB. The rotation, deformation and incision of T1 (Figure 7) suggests it was originally more extensive. The instability and remobilisation are probably related to a phase of erosion prior to deposition of P2. This indicates that the NSB was active prior to the deposition of P2, which is supported by the different depths of incision of the NSB and SSB. The NSB incision is *ca* 15 m shallower than the SSB, and had they been contemporaneous, the SSB would have had a significant gradient advantage over the NSB, with the majority of flows transported through the SSB. This may suggest that the NSB incised and filled prior to the incision by the SSB (Figure 10Ai). The two channels may have formed from an up-dip avulsion, or by two separate channel systems (Figure 10Aii). Channel avulsion can be triggered by a number of factors, including changes in slope gradient, channel aggradation and reduced channel relief, continued deformation of the MTD resulting in breaching of confinement, and channel plugging through MTD deposition (Armitage et al., 2012; Kolla, 2007; Ortiz Karpf et al., 2015; Posamentier, 2003). A number of these mechanisms can be discounted; there is no evidence for the large scours or rapid deposition associated with a change in slope at this stratigraphic level. If channel plugging were responsible, evidence of confined or partially confined flows (as seen in P4) would be expected, and no evidence of syn-sedimentary deformation (such as localised faulting, thinning or thickening of deposits away from the area of deformation, or deformation of deposits) is visible. One possible mechanism is channel avulsion resulting from in-channel aggradation (Figure 10Aii) that reduced channel relief, with the NSB representing the original channel, and the SSB the post-avulsion channel (Figure 10Aiii,iv). In this scenario, the 40 m of coarse-grained sandstone above the basal conglomerates would be the product of the channel adjusting towards equilibrium (Kneller, 2003). An alternative mechanism is that a headward eroding channel developed from the toe of the basin-facing slope of the MTD, and eroded deeper, thus achieving a gradient advantage.

Alternatively, it may be the case that the NSB and SSB were coeval. Subtle variations in channel morphology and thalweg gradient can influence flow velocity, and thus the erosion-deposition threshold (Kneller, 1995; Stevenson et al., 2015). A steeper gradient in the SSB would result in more sediment bypass through this channel, whilst deposition occurred in the NSB (Figure 10Bi). When available accommodation within the NSB was filled, all flows would be diverted down the SSB (Figure 10Bii), which begins to aggrade (Figure 10Biii). A further possibility is that NSB and SSB could represent two channel systems that developed above the MTD independently, but in close proximity, as seen beyond the shelf-edge delta in the Fuji-Einstein system (Gulf of Mexico, Sylvester et al., 2012). The transition from erosion and bypass to aggradation within the NSB suggests a waning sediment supply, with depositional flows having limited ability to erode and form new conduits, meaning channel development would probably be coeval in this scenario.

5.5.1 | Knickpoint-induced channelisation

The depth of incision (>75 m), steep sides (up to 70°) of the erosive surface, and low aspect ratio (estimated width/depth <*ca* 7–9 by doubling mapped width to account for the fault), all suggest that incision dominated over lateral erosion. The presence of multiple terrace surfaces suggests that this incision took place in a series of discrete phases. Furthermore, in the SSB, the basal deposits of terraces T2 and T3 consist of thin beds composed of fine to medium-grained sandstones, underlain by pebbly sandstones and conglomerates (up to 0.4–0.8 m thick in T3) directly above erosion surfaces. The pebbly sandstones and conglomerates are interpreted as bedload-derived channel lag deposits that probably took a long time to accumulate, whilst the abrupt change to thin beds deposited from suspension suggests rapid episodes of incision. Taken together with the stepped nature of the composite basal erosion surface, these periods of rapid erosion may have been on the order of 10 m or greater.
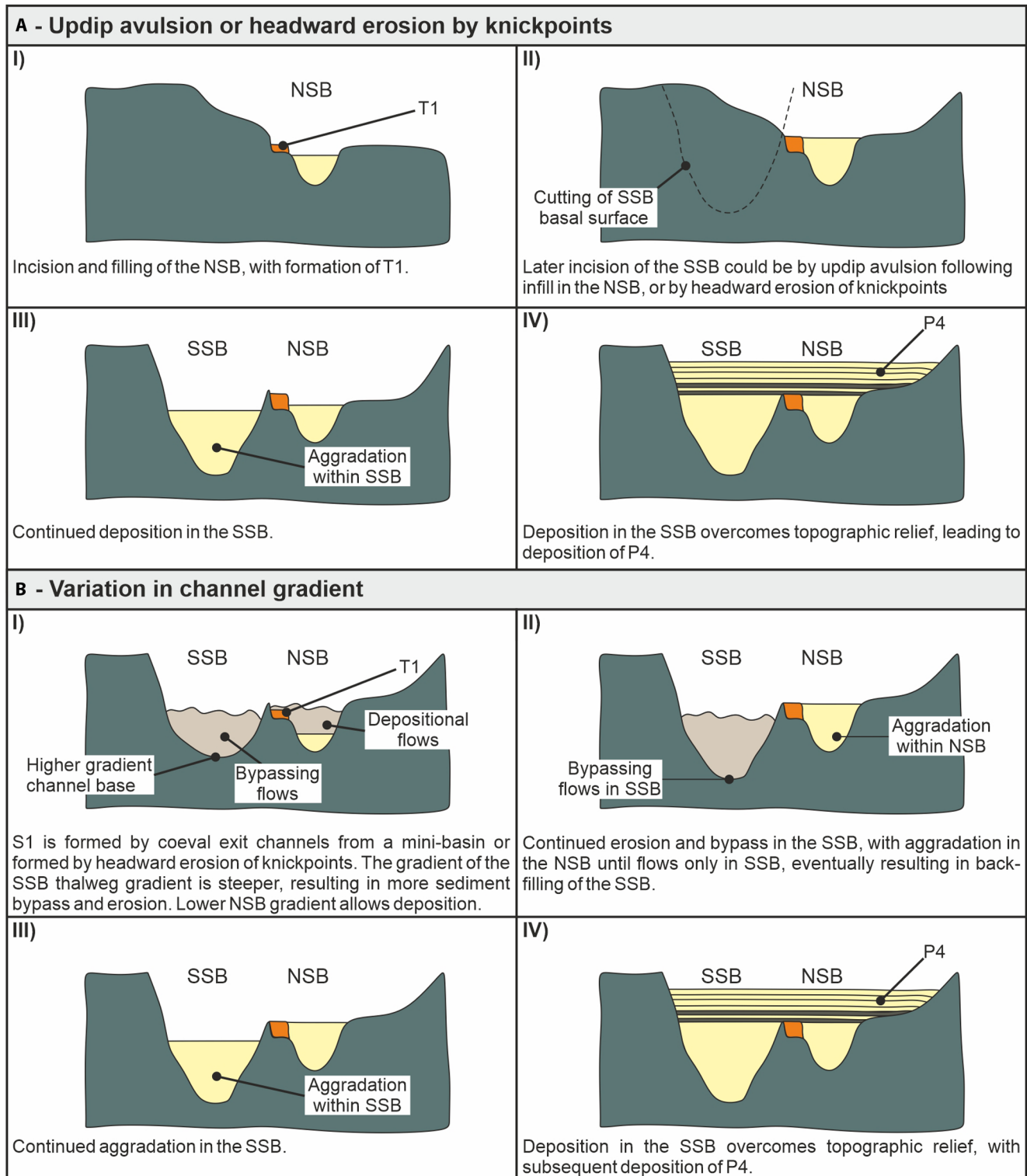
A - Updip avulsion or headward erosion by knickpoints

I) NSB — T1

Incision and filling of the NSB, with formation of T1.

II) NSB

Cutting of SSB basal surface

Later incision of the SSB could be by updip avulsion following infill in the NSB, or by headward erosion of knickpoints

III) SSB NSB

Aggradation within SSB

Continued deposition in the SSB.

IV) SSB NSB P4

Deposition in the SSB overcomes topographic relief, leading to deposition of P4.

B - Variation in channel gradient

I) SSB NSB T1

Depositional flows

Higher gradient channel base Bypassing flows

S1 is formed by coeval exit channels from a mini-basin or formed by headward erosion of knickpoints. The gradient of the SSB thalweg gradient is steeper, resulting in more sediment bypass and erosion. Lower NSB gradient allows deposition.

II) SSB NSB

Aggradation within NSB

Bypassing flows in SSB

Continued erosion and bypass in the SSB, with aggradation in the NSB until flows only in SSB, eventually resulting in back-filling of the SSB.

III) SSB NSB

Aggradation within SSB

Continued aggradation in the SSB.

IV) SSB NSB P4

Deposition in the SSB overcomes topographic relief, with subsequent deposition of P4.

FIGURE 10 Evolutionary development of the two channels and their formative processes. (A) Incisional avulsion, where S1 formed in two stages. First NSB is cut and filled. Then later incision of the SSB, which could be formed by up-dip avulsion following the infill in the NSB. Or alternatively, it could be formed by headward erosion of knickpoints (see text for details). (B) The NSB and SSB represent coetaneous exit channels from a mini-basin, with the NSB having a lower thalweg gradient. Such coetaneous channels could originally have been formed, or enhanced, by headward eroding knickpoints. The high gradient in the SSB causes total bypass of flows, with deposition in the NSB. Once aggradation within the NSB exceeds the generation of accommodation, flows are transported down the SSB, which subsequently backfills

This raises the question as to what process(es) would lead to such a rapid and repeated decrease in local base-level? Given that these channels are cut into a >200 m thick MTD, then there is probably substantial relief, and commensurate high gradients, on the basin-facing slope of the landslide (Martínez-Doñate et al., 2021; Steventon et al., 2019). Flows traversing such steep slopes are known to be associated with upstream migrating knickpoints (Tek et al., 2021), and knickpoint heights can be >10 m in submarine channels (Gales et al., 2019; Guiastrennec-Faugas et al., 2020, 2021; Heijnen et al., 2020). This suggests that the data are consistent with several discrete phases of knickpoint erosion, separated by sufficient time for lag deposits to accumulate; these lag deposits becoming terrace surfaces following the next incision phase (cf. Heiniö & Davies, 2007). These individual phases of knickpoint erosion probably consist of multiple knickpoints, potentially in knickpoint zones (Guiastrennec-Faugas et al., 2020, 2021; Heijnen et al., 2020; Tek et al., 2021). In turn, this suggests that the adjustment towards channel equilibrium takes place via a series of episodic knickpoint periods.

Little direct information is available on the location of the NSB and SSB with respect to the large-scale morphology of the MTD body. The varying degrees of sandstone block disaggregation, thickness of the MTD and the lack of evidence of compressional thrust faulting suggests that the channels incise in the translational zone of the MTD body. However, the presence of multiple knickpoints might reflect the large-scale topography and small-scale rugosity of the top surface of a basin-facing slope of the submarine landslide. The close association of the two channels also suggests that knickpoints can lead to the formation of multiple conduits, either coevally (Figure 10Bi), or via headward erosion of a new channel (Figure 10Aii,iii; Gales et al., 2019). Potentially, buried megaclasts could have formed lithological contrasts, and influenced surface sediment routes (Alves & Cartwright, 2010; Ward et al., 2018). Here, the sedimentological record of these episodic knickpoint periods is restricted to the stepped (terraced) and narrow conduit, the bedload lag deposits stranded on these terrace surface, and the abrupt facies change on top of the lag deposits. This contrasts with studies of modern systems that have also recognised extensive aggradational deposits, including bedforms, across and downstream of knickpoints (Chen et al., 2021; Guiastrennec-Faugas et al., 2021). Such deposits have been identified from flows cutting into previously deposited sand-rich deposits, rather than in cases such as this where the erosion is into mud-rich MTDs. The basal erosion surfaces in the La Peña channel also show extensive grooves formed by flows with significant cohesive strength such as debris flows, or the debritic flow components of hybrid beds (Baas et al., 2021; Peakall et al., 2020). These

may either represent direct erosion associated with the knickpoints, or later erosion after the passage of knickpoints, but they do raise the question as to whether mud-rich flows, such as debris flows, may be associated with knickpoints. A channel readjusting its profile towards equilibrium, across a mud-rich MTD with large amounts of relief, is probably associated with mud-rich transitional flows (*sensu* Baas et al., 2009) that may potentially develop into debris flows at the head where erosion is most concentrated (Baas et al., 2021). Consequently, a wide range of flow rheologies might be expected across knickpoints in such settings, in marked contrast to most of the modern systems in which knickpoints have been studied to date. The present study thus identifies evidence for knickpoints from the geometry of the conduit, and the sediments immediately overlying it, and suggests that knickpoint process dynamics in submarine systems may be more diverse than presently recognised.

6 | CONCLUSIONS

Two exceptionally well-exposed erosional channel systems (the NSB and SSB) that incised into a thick MTD and document the formation and flow-scale evolution of a seismic-scale outcrop are presented, using sedimentological analysis, geological mapping and photogrammetric modelling. The La Peña channels are erosively confined, high percentage sandstone systems, overlain by a confined prograding lobe complex that developed within the large-scale erosion surface. The ability of flows to progressively incise >75 m into an underlying MTD, with margins of up to 70°, is demonstrated. The progressive incision is suggested to record episodic periods of headward erosion by multiple knickpoints that developed above the basinward dip surface of the underlying MTD. Development of lag deposits on surfaces that later formed terraces indicates considerable time in between these periods of knickpoint erosion, perhaps reflecting the large-scale topography and small-scale rugosity of the basin-facing slope of the submarine landslide. Aggradational stacking of sand-rich channel-fill, exhibiting a high degree of homogeneity, marks the evolution from erosion and sediment bypass to deposition. Above this, stepped changes in confinement coincided with a change in intrachannel architecture to laterally migrating channel bodies, followed by tabular, highly aggradational fill. Progradation of a lobe complex within the larger channel erosion surface is shown, characterised by a lack of compensational stacking and increasingly thick deposits of proximal lobe hybrid bed deposits. Overlying this, an up-dip avulsion induced lobe switching and back-stepping relative to previous deposition,

and subsequent failure of a sandstone body up-dip, that led to emplacement of a sandstone-rich MTD within the conduit. Collectively, these deposits are argued to represent the product of episodic knickpoint-driven erosion, and subsequent infill, across a large-scale MTD. The depositional signature of these interpreted knickpoints is markedly different from existing models of knickpoint deposits based on in-channel erosion of existing sand-rich deposits, but is likely reflective of other highly erosional settings undergoing large-scale slope adjustment.

CONFLICT OF INTEREST
There are no conflicts of interest in the preparation or publication of this work.

DATA AVAILABILITY STATEMENT
The data that support the findings of this study are available from the corresponding author upon reasonable request.

ORCID
David M. Hodgson https://orcid.org/0000-0003-3711-635X

REFERENCES
Allen, J.R.L. (1984) Parallel lamination developed from upper-stage plane beds: a model based on the larger coherent structures of the turbulent boundary layer. *Sedimentary Geology*, 39, 227–242. 10.1016 /0037-0738 (84)90052 -6.

Alves, T.M. (2015) Submarine slide blocks and associated soft-sediment deformation in deep-water basins: a review. *Marine and Petroleum Geology*, 67, 262–285.

Alves, T.M. & Cartwright, J.A. (2010) The effect of mass-transport deposits on the younger slope morphology, offshore Brazil. *Marine and Petroleum Geology*, 27, 2027–2036.

Armitage, D.A., McHargue, T., Fildani, A. & Graham, S.A. (2012) Postavulsion channel evolution: Niger Delta continental slope. *AAPG Bulletin*, 96, 823–843.

Astini, R.A., Benedetto, J.L. & Vaccari, N.E. (1995) The Early Paleozoic evolution of the Argentine Precordillera as a Laurentian rifted, drifted and collided terrane: a geo- dynamic model. *GSA Bulletin*, 107, 253–273.

Baas, J.H., Best, J.L., Peakall, J. & Wang, M. (2009) A phase diagram for turbulent, transitional, and laminar clay suspension flows. *Journal of Sedimentary Research*, 79, 162–183.

Baas, J.H., Tracey, N.D. & Peakall, J. (2021) Sole marks reveal deep-marine depositional process and environment: implications for flow transformation and hybrid event bed models. *Journal of Sedimentary Research*, 91, 986–1009.

Babonneau, N., Savoye, B., Cremer, M. & Bez, M. (2004) Multiple terraces within the deep incised Zaire Valley (ZaïAngo Project): are they confined levees? In: Lomas, S.A. & Joseph, P. (Eds.), *Confined Turbidite Systems. Geological Society, London, Special Publications 222*, 91–114.

Babonneau, N., Savoye, B., Cremer, M. & Bez, M. (2010) Sedimentary architecture in meanders of a submarine channel: detailed study of the present Congo turbidite channel (ZAIANGO project). *Journal of Sedimentary Research*, 80, 852–866.

Babonneau, N., Savoye, B., Cremer, M. & Klein, B. (2002) Morphology and architecture of the present canyon and channel system of the Zaire deep-sea fan. *Marine and Petroleum Geology*, 19, 445–467.

Bart, P.J., De Batist, M. & Jokat, W. (1999) Interglacial collapse of Crary trough-mouth fan, Weddell Sea, Antarctica: implications for Antarctic glacial history. *Journal of Sedimentary Research*, 69, 1276–1289.

Best, J. & Bridge, J. (1992) The morphology and dynamics of low amplitude bedwaves upon upper stage plane beds and the preservation of planar laminae. *Sedimentology*, 39, 737–752.

Bouma, A. (1962) *Sedimentology of some flysch deposits: a graphic approach to facies interpretation.* Amsterdam/New York: Elsevier, 168 pp.

Brooks, H.L., Hodgson, D.M., Brunt, R.L., Peakall, J., Hofstra, M. & Flint, S.S. (2018) Deep-water channel-lobe transition zone dynamics: processes and depositional architecture, an example from the Karoo Basin, South Africa. *GSA Bulletin*, 130, 1723–1746.

Bull, S., Browne, G.H., Arnot, M.J. & Strachan, L.J. (2020) Influence of Mass Transport Deposit (MTD) surface topography on deep-water deposition: an example from a predominantly fine-grained continental margin, New Zealand. In: Georgiopoulou, A., Amy, L.A., Benetti, S., Chaytor, J.D., Clare, M.A., Gamboa, D., Haughton, P.D.W., Moernaut, J. & Mountjoy, J.J. (Eds.), *Subaqueous mass movements and their consequences: advances in process understanding, monitoring and hazard assessments. Geological Society, London, Special Publications*, 500, 147–171.

Chen, Y., Parsons, D.R., Simmons, S.M., Williams, R., Cartigny, M.J.B., Hughes Clarke, J.E., Stacey, C.D., Hage, S., Talling, P.J., Azpiroz-Zabala, M., Clare, M.A., Hizzett, J.L., Heijnen, M.S., Hunt, J.E., Lintern, D.G., Sumner, E.J., Vellinga, A.J. & Vendettuoli, D. (2021) Knickpoints and crescentic bed-form interactions in submarine channels. *Sedimentology*, 68, 1358–1377.

Constantine, J.A., Dunne, T., Piégay, H. & Kondolf, G.M. (2010) Controls on the alluviation of oxbow lakes by bed-material load along the Sacramento River, California. *Sedimentology*, 57, 389–407.

Deptuck, M.E., Steffens, G.S., Barton, M. & Pirmez, C. (2003) Architecture and evolution of upper fan channel belts on the Niger Delta slope and in the Arabian Sea. *Marine and Petroleum Geology*, 20, 649–676.

Dott, J. (1963) Dynamics of subaqueous gravity depositional processes. *AAPG Bulletin*, 47(1), 104–128.

Dykstra, M., Garyfalou, K., Kertznus, V., Kneller, B., Milana, J.P., Molinaro, M., Szuman, M. & Thompson, P. (2011) Mass-transport deposits: combining outcrop studies and seismic forward modeling to understand lithofacies distributions,

deformation and their seismic expression. In: Shipp, R.C., Weimer, P. & Posamentier, H.W. (Eds.) *Mass-transport deposits in deepwater settings. SEPM Special Publications*, *96*, 293–310.

Elverhøi, A., Hooke, R.L.B. & Solheim, A. (1998) Late Cenozoic erosion and sediment yield from the Svalbard-Barents Sea region: implications for understanding erosion of glacierized basins. *Quaternary Science Reviews*, *17*, 209–241.

Eschard, R., Albouy, E., Deschamps, R., Euzen, T. & Ayub, A. (2003) Downstream evolution of turbiditic channel complexes in the Pab Range outcrops (Maastrichtian, Pakistan). *Marine and Petroleum Geology*, *20*(6–8), 691–710.

Fallgatter, C., Kneller, B., Paim, P.S.G. & Milana, J.P. (2017) Transformation, partitioning and flow-deposit interactions during the run-out of megaflows. *Sedimentology*, *64*, 359–387.

Fernández-Seveso, F. & Tankard, A.J. (1995) Tectonics and stratigraphy of the late Paleozoic Paganzo Basin of Western Argentina and its regional implications. In: Tankard, A.J., Suarez, S. & Welsink, H.J. (Eds.), *Petroleum basins of South America. AAPG Memoirs 62*, 285–301.

Fisk, H.N. (1947) *Fine grained alluvial deposits and their effect on Mississippi River activity, Volumes 1 & 2*. Mississippi River Commission: Vicksburg, MS.

Fonnesu, M., Haughton, P., Felletti, F. & McCaffrey, W. (2015) Short length-scale variability of hybrid event beds and its applied significance. *Marine and Petroleum Geology*, *67*, 583–603.

Gales, J.A., Talling, P.J., Cartigny, M.J.B., Hughes Clarke, J., Lintern, G., Stacey, C. & Clare, M.A. (2019) What controls submarine channel development and the morphology of deltas entering deep-water fjords? *Earth Surface Processes and Landforms*, *44*, 535–551.

Gardner, M.H., Borer, J.M., Melik, J.J., Mavilla, N., Dechesne, M. & Wagerle, R.D. (2003) Stratigraphic process-response model for submarine channels and related features from studies of Permian Brushy Canyon outcrops, West Texas. *Marine and Petroleum Geology*, *20*, 757–788.

Guiastrennec-Faugas, L., Gillet, H., Jacinto, R.S., Dennielou, B., Hanquiez, V., Schmidt, S., Simplet, L. & Rousset, A. (2020) Upstream migrating knickpoints and related sedimentary processes in a submarine canyon from a rare 20-year morpho-bathymetric time-lapse (Capbreton submarine canyon, Bay of Biscay, France). *Marine Geology*, *423*, 106143.

Guiastrennec-Faugas, L., Gillet, H., Peakall, J., Dennielou, B., Gaillot, A. & Jacinto, R.S. (2021) Initiation and evolution of knickpoints and their role in cut and fill processes in active submarine channels. *Geology*, *49*, 314–319.

Hansen, L.A.S., Callow, R.H.T., Kane, I.A., Gamberi, F., Rovere, M., Cronin, B.T. & Kneller, B.C. (2015) Genesis and character of thin-bedded turbidites associated with submarine channels. *Marine and Petroleum Geology*, *67*, 852–879.

Hansen, L.A.S., Callow, R., Kane, I.A. & Kneller, B.C. (2017a) Differentiating submarine channel related thin-bedded turbidite facies: outcrop example from the Rosario Formation, Mexico. *Sedimentary Geology*, *358*, 19–34.

Hansen, L.A.S., Janocko, M., Kane, I. & Kneller, B. (2017b) Submarine channel evolution, terrace development, and preservation of intra-channel thin-bedded turbidites: Mahin and Avon channels, offshore Nigeria. *Marine Geology*, *383*, 146–167.

Haughton, P.D., Barker, S.P. & McCaffrey, W.D. (2003) 'Linked' debrites in sand-rich turbidite systems–origin and significance. *Sedimentology*, *50*(3), 459–482.

Haughton, P., Davis, C., McCaffrey, W. & Barker, S. (2009) Hybrid sediment gravity flow deposits–classification, origin and significance. *Marine and Petroleum Geology*, *26*(10), 1900–1918.

Heijnen, M.S., Clare, M.A., Cartigny, M.J.B., Talling, P.J., Hage, S., Lintern, D.G., Stacey, C., Parsons, D.R., Simmons, S.M., Chen, Y., Sumner, E.J., Dix, J.K. & Hughes Clarke, J.E. (2020) Rapidly-migrating and internally-generated knickpoints can control submarine channel evolution. *Nature Communications*, *11*, 3129.

Heiniö, P. & Davies, R.J. (2007) Knickpoint migration in submarine channels in response to fold growth, western Niger Delta. *Marine and Petroleum Geology*, *24*, 434–449.

Hiscott, R.N. (1981) Deep sea fan deposits in the Macigno Formation (Middle-Upper Oligocene) of the Gordana Valley, Northern Apennines, Italy: discussion. *Journal of Sedimentary Petrology*, *51*, 1015–1021.

Hiscott, R.N., Hall, F.R. & Pirmez, C. (1997) Turbidity current overspill form the Amazon Channel: texture of the silt/sand load, palaeoflow from anisotropy of magnetic susceptibility, and implications for flow processes. In: Flood, R.D., Piper, D.J.W., Klaus, A. & Peterson, L.C. (Eds.), *Proceedings of the Ocean Drilling Programme, Scientific Results, Leg 155*. Ocean Drilling Programme, College Station, TX, pp. 53–78.

Hodgson, D.M. (2009) Distribution and origin of hybrid beds in sand-rich submarine fans of the Tanqua depocentre, Karoo Basin, South Africa. *Marine and Petroleum Geology*, *26*, 1940–1956. https://doi.org/10.1016/j.marpetgeo.2009.02.011

Hodgson, D.M., Di Celma, C.N., Brunt, R.L. & Flint, S.S. (2011) Submarine slope degradation and aggradation and the stratigraphic evolution of channel–levee systems. *Journal of the Geological Society of London*, *168*, 625–628.

Hodgson, D.M. & Haughton, P.D.W. (2004) Impact of syn-depositional faulting on gravity current behaviour and deep-water stratigraphy: Tabernas–Sorbas Basin, SE Spain. In: Lomas, S. & Joseph, P. (Eds.), *Confined turbidites systems. Geological Society, London, Special Publications*, *222*, 135–158.

Hodgson, D.M., Kane, I.A., Flint, S.S., Brunt, R.L. & Ortiz-Karpf, A. (2016) Time-transgressive confinement on the slope and the progradation of basin-floor fans: implications for the sequence stratigraphy of deep-water deposits. *Journal of Sedimentary Research*, *86*, 73–86. https://doi.org/10.2110/jsr.2016.3

Hofstra, M., Peakall, J., Hodgson, D.M. & Stevenson, C.J. (2018) Architecture and morphodynamics of subcritical sediment waves in an ancient channel–lobe transition zone. *Sedimentology*, *65*, 2239–2367. https://doi.org/10.1111/sed.12468

Hubbard, S.M., Covault, J.A., Fildani, A. & Romans, B.W. (2014) Sediment transfer and deposition in slope channels: deciphering the record of enigmatic deep-sea processes from outcrop. *GSA Bulletin*, *126*, 857–871.

Jegou, I., Savoye, B., Pirmez, C. & Droz, L. (2008) Channel-mouth lobe complex of the recent Amazon Fan: the missing piece. *Marine Geology*, *252*, 62–77.

Jobe, Z.R., Lowe, D.R. & Morris, W.R. (2012) Climbing-ripple successions in turbidite systems: depositional environments, sedimentation rates and accumulation times. *Sedimentology*, *59*(3), 867–898.

Kane, I.A. & Hodgson, D.M. (2011) Sedimentological criteria to differentiate submarine channel levee sub-environments: exhumed

examples from the Rosario Fm. (Upper Cretaceous) of Baja California, Mexico, and the Fort Brown Fm. (Permian), Karoo Basin, S. Africa. *Marine and Petroleum Geology*, 28, 807–823.

Kane, I.A. & Pontén, A.S.M. (2012) Submarine transitional flow deposits in the Paleogene Gulf of Mexico. *Geology*, 40, 1119–1122. https://doi.org/10.1130/G33410.1

Kneller, B. (1995) Beyond the turbidite paradigm, physical models for deposition of turbidites and their implications for reservoir prediction. In: Hartley, A.J. & Prosser, D.J. (Eds.), *Characterization of Deep-Marine Clastic Systems. Geological Society, London, Special Publications*, 94, 31–49.

Kneller, B. (2003) The influence of flow parameters on turbidite slope channel architecture. *Marine and Petroleum Geology*, 20, 901–910.

Kneller, B.C. & Branney, M.J. (1995) Sustained high-density turbidity currents and the deposition of thick massive sands. *Sedimentology*, 42, 607–616.

Kneller, B., Dykstra, M., Fairweather, L. & Milana, J.P. (2016) Mass-transport and slope accommodation: implications for turbidite sandstone reservoirs. *AAPG Bulletin*, 100, 213–235.

Kneller, B.C., Edwards, D., McCaffrey, W. & Moore, R. (1991) Oblique reflection of turbidity currents. *Geology*, 19, 250–252.

Kneller, B. & McCaffrey, W. (1999) Depositional effects of flow nonuniformity and stratification within turbidity currents approaching a bounding slope: deflection, reflection, and facies variation. *Journal of Sedimentary Research*, 69, 980–991.

Kolla, V. (2007) A review of sinuous channel avulsion patterns in some major deep-sea fans and factors controlling them. *Marine and Petroleum Geology*, 24, 450–469.

Kremer, C.H., McHargue, T., Scheucher, L. & Graham, S.A. (2018) Transversely-sourced mass-transport deposits and stratigraphic evolution of a foreland submarine channel system: deep-water Tertiary strata of the Austrian Molasse Basin. *Marine and Petroleum Geology*, 92, 1–19.

Limarino, C.O., Cesari, S.N., Net, L.I., Marenssi, S.A., Gutierrez, R.P. & Tripaldi, A. (2002) The Upper Carboniferous postglacial transgression in the Paganzo and Rio Blanco basins (northwestern Argentina): facies and stratigraphic significance. *Journal of South American Earth Sciences*, 15(4), 445–460. https://doi.org/10.1016/S0895-9811(02)00048-2

Limarino, C.O., Tripaldi, A., Marenssi, S. & Fauque, L. (2006) Tectonic, sea level and climatic controls on Late Palaeozoic sedimentation in the western basins of Argentina. *Journal of South American Earth Sciences*, 22, 205–226.

López-Gamundí, O. & Martínez, M. (2000) Evidence of glacial abrasion in the Calingasta Uspallata and western Paganzo basins, mid-Carboniferous of western Argentina. *Palaeogeography, Palaeoclimatology, Palaeoecology*, 159, 145–165.

Lowe, D.R. (1982) Sediment gravity flows: II. Depositional models with special reference to the deposits of high-density turbidity currents. *Journal of Sedimentary Petrology*, 52, 279–297.

Lowe, D.R. (1988) Suspended-load fallout rate as an independent variable in the analysis of current structures. *Sedimentology*, 35, 765–776.

Macdonald, H.A., Peakall, J., Wignall, P.B. & Best, J. (2011) Sedimentation in deep-sea lobe-elements: implications for the origin of thickening-upward sequences. *Journal of the Geological Society*, 168, 319–331.

Mantz, P.A. (1978) Bedforms produced by fine, cohesionless, granular and flakey sediments under subcritical water flows. *Sedimentology*, 25, 83–103.

Marini, M., Felletti, F., Milli, S. & Patacci, M. (2016) The thick-bedded tail of turbidite thickness distribution as a proxy for flow confinement: examples from tertiary basins of central and northern Apennines (Italy). *Sedimentary Geology*, 341, 96–118.

Martínez-Doñate, A., Privat, A.L., Hodgson, D.M., Jackson, C.L., Kane, I.A., Spychala, Y.T., Duller, R.A., Stevenson, C., Keavney, E., Schwarz, E. & Flint, S.S. (2021) Substrate entrainment, depositional relief, and sediment capture: Impact of a submarine landslide on flow process and sediment supply. *Frontiers in Earth Science*, 9, 757617.

Masalimova, L.U., Lowe, D.R., Sharman, G.R., King, P.R. & Arnot, M.J. (2016) Outcrop characterization of a submarine channel-lobe complex: the lower Mount Messenger Formation, Taranaki Basin, New Zealand. *Marine and Petroleum Geology*, 71, 360–390.

McArthur, A., Kane, I.A., Bozetti, G., Hansen, L.A.S. & Kneller, B.C. (2019) Supercritical flows overspilling from bypass-dominated submarine channels and the development of overbank bedforms. *The Depositional Record*, 6, 21–40.

Milana, J.P., Kneller, B. & Dykstra, M. (2010) Mass-transport deposits and turbidites, syn- to-post-glacial carboniferous basins of Western Argentina. ISC 2010 Field Guide, 01–88.

Milliman, J.D. & Meade, R.H. (1983) World-wide delivery of river sediment to the oceans. *The Journal of Geology*, 91, 1–21.

Morris, E.A., Hodgson, D.M., Flint, S.S., Brunt, R.L., Butterworth, P.J. & Verhaeghe, J. (2014) Sedimentology, stratigraphic architecture, and depositional context of submarine frontal-lobe complexes. *Journal of Sedimentary Research*, 84, 763–780.

Moscardelli, L., Wood, L. & Mann, P. (2006) Mass-transport complexes and associated processes in the offshore area of Trinidad and Venezuela. *AAPG Bulletin*, 90, 1059–1088.

Mpodozis, C. & Ramos, V.A. (1989) The Andes of Chile and Argentina. In: Ericksen, G.E., Cañas Pinochet, M.T. & Reinemud, J.A. (Eds.), *Geology of the Andes and its relations to hydrocarbon and mineral resources*. Circum-Pacific Council for Energy and Mineral Resources, Earth Science Series, 11, 59–90.

Mulder, T. & Alexander, J. (2001) The physical character of subaqueous sedimentary density flows and their deposits. *Sedimentology*, 48, 269–299.

Mulder, T., Zaragosi, S., Razin, P., Grelaud, C., Lanfumy, V. & Bavoil, F. (2009) A new conceptual model for the deposition process of homogenite: application to a Cretaceous megaturbidite of the western Pyrenees (Basque region, SW France). *Sedimentary Geology*, 222, 263–273.

Mutti, E. (1984) The Hecho Eocene submarine fan system, south-central Pyrenees, Spain. *Geo Marine Letters*, 3, 199–202. https://doi.org/10.1007/BF02462468

Mutti, E. (1992) Turbidite Sandstones. Agip-Instituto di Geologia, Università di Parma, Italy, 275 p.

Mutti, E. & Normark, W.R. (1987) Comparing examples of modern and ancient turbidite systems, problems and concepts. In: Leggett, J.K. & Zuffa, G.G. (Eds.) *Marine clastic sedimentology, concepts and case studies*. London, UK: Graham and Trotman, London, pp. 1–37.

Mutti, E. & Ricci Lucci, F. (1972). Le turbidite dell' Appenino Setlentrionale: introduzione all' analisi di facies, vol. 11. Società

Geologica Italiana, Memorie (1978 English translation by T.H. Nilsen). *International Geological Review*, **20**, 125-166. 161-199.

Mutti, E., Tinterri, R., Benevelli, G., di Biase, D. & Cavanna, G. (2003) Deltaic, mixed and turbidite sedimentation of ancient foreland basins. *Marine and Petroleum Geology*, **20**(6–8), 733–755.

Nardin, T.R., Hein, F.J., Gorsline, D.S. & Edwards, B.D. (1979) A review of mass movement processes, sediment and acoustic characteristics, and contrasts in slope and base-of-slope systems versus canyon-fan-basin floor systems. In: Doyle, L.J. & Pilkey, O.H. (Eds.), *Geology of continental slopes. SEPM Society for Sedimentary Geology*, Special Publication 27, 61–73.

Nelson, C.H., Escutia, C., Damuth, J.E. & Twichell, D.C. (2011) Interplay of mass-transport and turbidite-system deposits in different active tectonic and passive continental margin settings: external and local controlling factors. In: Shipp, R.C., Weimer, P. & Posamentier, H.W. (Eds.), *Mass-transport deposits in deepwater settings. SEPM Society for Sedimentary Geology*, 39–66.

Normark, W.R. & Damuth, J.E. the Leg 155 Sedimentology Group (1997) Sedimentary facies and associated depositional elements of the Amazon Fan. In: Flood, R.D., Piper, D.J.W., Klaus, A. & Peterson, L.C. (Eds.), *Proceedings of the Ocean Drilling Programme, Scientific Results*, Leg 155. Ocean Drilling Programme, College Station, TX, pp. 611–651.

Ortiz-Karpf, A., Hodgson, D.M. & McCaffrey, W.D. (2015) The role of mass-transport complexes in controlling channel avulsion and the subsequent sediment dispersal patterns on an active margin: the Magdalena Fan, offshore Colombia. *Marine and Petroleum Geology*, **64**, 58–75.

Pazos, P.J. (2002) The Late Carboniferous glacial to postglacial transition; facies and sequence stratigraphy, western Paganzo Basin, Argentina. *Gondwana Research*, **5**, 467–487.

Peakall, J., Ashworth, P.J. & Best, J.L. (2007) Meander bend evolution, alluvial architecture, and the role of cohesion in sinuous river channels: a flume study. *Journal of Sedimentary Research*, **77**, 197–212.

Peakall, J., Best, J., Baas, J.H., Hodgson, D.M., Clare, M.A., Talling, P.J., Dorrell, R.M. & Lee, D.R. (2020) An integrated process-based model of flutes and tool marks in deep- water environments: implications for palaeohydraulics, the Bouma sequence and hybrid event beds. *Sedimentology*, **67**, 1601–1666.

Pett, J.W. & Walker, R.G. (1971) Relationship of flute cast morphology to internal sedimentary structures in turbidites. *Journal of Sedimentary Petrology*, **41**, 114–128.

Pickering, K.T., Hiscott, R.N. & Hein, F.J. (1989) *Deep-marine environments*. London: Unwin Hyman, 416 pp.

Piper, D.J.W. & Normark, W.R. (1983) Turbidite depositional patterns and flow characteristics, Navy submarine fan, California Borderland. *Sedimentology*, **30**, 681–694.

Piper, D.J.W., Pirmez, C., Manley, P.L., Long, D., Flood, R.D., Normark, W.R. & Showers, W. (1997) Mass transport deposits of the Amazon Fan. In: Flood, R.D., Piper, D.J., Klaus, A. & Peterson, L.C. (Eds.) *Proceedings or the Ocean Drilling Program, Scientific Results, Amazon Fan 155*. College Station, TX: Ocean Drilling Program, pp. 109–146.

Pirmez, C. & Flood, C. (1995) Morphology and structure of Amazon channel. In: Flood, R.D., Piper, D.J.W., Klaus, A. & Peterson, L.C. (Eds.), *Proceedings of the Ocean Drilling Program, Initial Reports 155*. Ocean Drilling Program, College Station, TX, 23–45.

Posamentier, H.W. (2003) Depositional elements associated with a basin- floor channel–levee system: case study from the Gulf of Mexico. *Marine and Petroleum Geology*, **20**, 667–690.

Prélat, A., Covault, J.A., Hodgson, D.M., Fildani, A. & Flint, S.S. (2010) Intrinsic controls on the range of volumes, morphologies, and dimensions of submarine lobes. *Sedimentary Geology*, **232**, 66–76. https://doi.org/10.1016/j.sedgeo.2010.09.010

Prélat, A., Hodgson, D.M. & Flint, S.S. (2009) Evolution, architecture and hierarchy of distributary deep-water deposits: a high-resolution outcrop investigation from the Permian Karoo Basin, South Africa. *Sedimentology*, **56**, 2132–2154.

Qin, Y.P., Alves, T.M., Constantine, J. & Gamboa, D. (2017) The role of mass wasting in the progressive development of submarine channels (Espirito Santo Basin, SE Brazil). *Journal of Sedimentary Research*, **87**, 500–516.

Ramos, V.A. (1988) The tectonics of central Andes; 30°–33°S latitude. In: Clark, S. & Burchfield, D. (Eds.), *Processes in continental lithosphere deformation. Geological Society of America, Special Paper*, **218**, 31–54.

Ramos, V.A., Jordan, T.E., Allmendinger, R.W., Mpodozis, C., Kay, S.M., Cortes, J.M. & Palma, M.A. (1986) Paleozoic terranes of the central Argentine-Chilean Andes. *Tectonics*, **5**, 855–880.

Rees, A.I. (1966) Some flume experiments with a fine silt. *Sedimentology*, **6**, 209–240.

Salfity, J.A. & Gorustovich, S.A. (1983) Paleogeografía de la Cuenca de Paganzo (Paleozoico Superior). *Revista Asociación Geológica Argentina*, **38**, 437–453.

Sinclair, H.D. & Tomasso, M. (2002) Depositional evolution of confined turbidite basins. *Journal of Sedimentary Research*, **72**, 451–456.

Sobiesiak, M.S., Alsop, G.I., Kneller, B. & Milana, J.P. (2017) Subseismic scale folding and thrusting within an exposed mass transport deposit: a case study from NW Argentina. *Journal of Structural Geology*, **96**, 176–191.

Sobiesiak, M., Kneller, B., Alsop, I.G. & Milana, J.P. (2016) Internal deformation and kinematic indicators within a tripartite mass transport deposit, NW Argentina. *Sedimentary Geology*, **344**, 364–381.

Southard, J.B. (1991) Experimental determination of bed-form stability. *Annual Review of Earth and Planetary Sciences*, **19**, 423–455.

Spychala, Y.T., Hodgson, D.M. & Lee, D.R. (2017b) Autogenic controls on hybrid bed distribution in submarine lobe complexes. *Marine and Petroleum Geology*, **88**, 1078–1093.

Spychala, Y.T., Hodgson, D.M., Prélat, A., Kane, I.A., Flint, S.S. & Mountney, N.P. (2017a) Frontal and lateral submarine lobe fringes: comparing facies, architecture and flow processes. *Journal of Sedimentary Research*, **87**, 1–21.

Stevenson, C.J., Jackson, C.-A.-L., Hodgson, D.M., Hubbard, S.M. & Eggenhuisen, J.T. (2015) Deep-water sediment bypass. *Journal of Sedimentary Research*, **85**(9), 1058–1081.

Steventon, M.J., Jackson, C.A.L., Hodgson, D.M. & Johnson, H.D. (2019) Strain analysis of a seismically imaged mass-transport complex, offshore Uruguay. *Basin Research*, **31**, 600–620.

Steventon, M.J., Jackson, C.-A.-L., Johnson, H.D., Hodgson, D.M., Kelly, S., Omma, J., Gopon, C., Stevenson, C. & Fitch, P. (2021) Evolution of a sand-rich submarine channel-lobe system and impact of mass-transport and transitional flow deposits on

reservoir heterogeneity: Magnus Field, northern North Sea. *Petroleum Geoscience.* https://doi.org/10.1144/petgeo2020-095

Stow, D.A.V. & Johansson, M. (2002) Deep-water massive sands: nature, origin and hydrocarbon implications. *Marine and Petroleum Geology*, 17, 145–174.

Sumner, E.J., Amy, L. & Talling, P.J. (2008) Deposit structure and processes of sand deposition from a decelerating sediment suspension. *Journal of Sedimentary Research*, 78, 529–547.

Sylvester, Z., Deptuck, M.E., Prather, B., Pirmez, C. & O'Byrne, C. (2012) Seismic stratigraphy of a shelf-edge delta and linked submarine channels in the NE Gulf of Mexico. In: Prather, B., Deptuck, M., Mohrig, B., Van Hoor, B. & Wynn, R.B. (Eds.), *Application of the principles of seismic geomorphology to continental slope and base-of-slope systems: case studies from seafloor and near-seafloor analogues. SEPM Society for Sedimentary Geology, Special Publication 99*, 31–59.

Talling, P.J., Amy, L.A., Wynn, R.B., Peakall, J. & Robinson, M. (2004) Beds comprising debrite sandwiched within co-genetic turbidite: origin and widespread occurrence in distal depositional environments. *Sedimentology*, 51, 163–194.

Talling, P.J., Masson, D.G., Sumner, E.J. & Malgesini, G. (2012) Subaqueous sediment density flows: depositional processes and deposit types. *Sedimentology*, 59, 1937–2003.

Tek, D.E., McArthur, A.D., Poyatos-Moré, M., Colombera, L., Patacci, M., Craven, B. & McCaffrey, W.D. (2021) Relating seafloor geomorphology to subsurface architecture: how mass-transport deposits and knickpoint-zones build the stratigraphy of the deep-water Hikurangi Channel. *Sedimentology*, 68, 3141–3190.

Tek, D.E., Poyatos-Moré, M., Patacci, M., McArthur, A.D., Colombera, L., Cullen, T.M. & McCaffrey, W.D. (2020) Syndepositional tectonics and mass-transport deposits control channelized, bathymetrically complex deep-water systems (Aínsa depocenter, Spain). *Journal of Sedimentary Research*, 90, 729–762.

Tinterri, R. (2011) Combined flow sedimentary structures and the genetic link between sigmoidal and hummocky cross-stratification. *GeoActa (Bologna)*, 10, 1–43.

Tinterri, R. & Muzzi Magalhaes, P. (2011) Syn-sedimentary structural control on foredeep turbidites: an example from Miocene Marnoso-arenacea Formation, Northern Apennines, Italy. *Marine and Petroleum Geology*, 28, 629–657.

Toonen, W.H.J., Kleinhans, M.G. & Cohen, K.M. (2012) Sedimentary architecture of abandoned channel fills. *Earth Surface Processes and Landforms*, 37, 459–472.

Valdez Buso, V., Milana, J.P., Sobiesiak, M.S. & Kneller, B. (2019) The Carboniferous MTD Complex at La Peña Canyon, Paganzo Basin (San Juan, Argentina). In: Otaga, K., Festa, A. & Pini, G.A. (Eds.), *Submarine landslides: subaqueous mass transport deposits from outcrops to seismic profiles.* Geophysical Monograph Series 246, 105-115.

Ward, I.P.N., Alves, M.T. & Blenkinsop, G.T. (2018) Submarine sediment routing over a blocky mass-transport deposit in the Espirito Santo Basin, SE Brazil. *Basin Research*, 30, 816–834.

Winn, R.D. & Dott, R.H. (1977) Large-scale traction structures in deep-water fan-channel conglomerates in southern Chile. *Geology*, 5, 41–44.

Wu, W., Li, Q., Yu, J., Lin, C., Li, D. & Yang, T. (2018) The Central Canyon depositional patterns and filling process in east of Lingshui Depression, Qiongdongnan Basin, northern South China Sea. *Geological Journal*, 53(6), 3064–3081.

Zavala, C. & Pan, S. (2018) Hyperpycnal flows and hyperpycnites: origin and distinctive characteristics. *Lithological Reservoirs*, 30, 1–27.

Zhao, X.M., Qi, K., Patacci, M., Tan, C.P. & Xie, T. (2019) Submarine channel network evolution above an extensive mass-transport complex: a 3D seismic case study from the Niger delta continental slope. *Marine and Petroleum Geology*, 104, 231–248.